THESIS FOR THE DEGREE OF LICENTIATE OF ENGINEERING

Optical Analysis and Characterisation of the Climate Research Instrument STEAMR

ARVID HAMMAR

Terahertz and Millimetre Wave Laboratory
Department of Microtechnology and Nanoscience - MC2
CHALMERS UNIVERSITY OF TECHNOLOGY
Göteborg, Sweden 2014

Optical Analysis and Characterisation of the Climate Research Instrument STEAMR
ARVID HAMMAR

Optical Analysis and Charectarisation of the Climate Research Instrument STEAMR
ARVID HAMMAR
Terahertz and Millimetre Wave Laboratory
Department of Microtechnology and Nanoscience - MC2
Chalmers University of Technology

Abstract

A growing interest for making high resolution observations in the upper troposphere and lower stratosphere has motivated the development of the multi-beam satellite-borne instrument Stratosphere-Troposphere Exchange And climate Monitor Radiometer (STEAMR). The measurements made by STEAMR will be used to monitor trace-gases and link the occurence of these to the Earth's climate by accurate modeling of the atmosphere. To interpret the measured data require a firm understanding of the coupling between the radiation emitted from the atmosphere to the signal being received by the instrument's optical system. Thus, precise knowledge of the instrument's optical performance while in orbit is crucial.

This thesis is dedicated to the study of optical analysis and measurements of the highly advanced optical system of the STEAMR instrument. A mechanical tolerance analysis of the complete optical system consisting of two polarisation separated focal plane arrays, a four reflector anastigmatic relay optics chain and an off-axis Ritchey-Chrétien telescope was performed. Using Monte-Carlo simulations in combination with ray-tracing and physical optics/physical theory of diffraction, it could be concluded that the overall reflector alignment accuracy from manufacturing should be better than 100 µm. Surface distortion analyses of the 1.6 m × 0.8 m primary reflector highlighted the need for an optical system with high stability in orbit (< 30 µm). Furthermore, it was shown that the manufacturing techniques were compliant with the requirements dictated by the tolerance analysis.

The design, manufacturing and characterisation of a 340 GHz smooth-walled spline feed horn antenna for STEAMR is presented also presented. Planar measurements of the amplitude and phase were performed at 329 and 338 GHz, where the corresponding coupling to the fundamental Gaussian beam mode was 97.7 and 97.8%, which is in excellent agreement with simulations.

ii

Acknowledgements

Being half-way toward my PhD degree, there is a number of people I want to thank for help-ing me reach this point. Firstly, I want to thank my supervisors Jan Stake and Anders Emrich for good discussions and support in many ways. I appreciate that I have been given the oppor-tunity to work on this interesting topic in a collaboration between Omnisys Instruments and Chalmers. I am thankful to Mark Whale who made a large contribution to the design of the STEAMR optics and who has always been helpful and encouraging since the first day I got involved in the project some three years ago. It has been fun working with Yogesh Karandikar who wrote the code for the smooth-walled spline horn optimisation and from whom I have learnt a lot about antennas in general through our many discussions. Steven McCallion and Per Forsberg have helped me with numerous practical issues and have supplied me with ex-cellent hardware. For that, I am grateful. Peter Sobis has helped me with countless things and has always been an overall good-guy; from the days I was working toward my MSc de-gree at Chalmers and up until today. In the same way have my former supervisor Sergey Cherednichenko and my office mate Vladimir Drakinskiy been helping me with many differ-ent things throughout these years. In the summer of 2013, William Hallberg helped with the initial near field scanning tests at 340 GHz, which I remember as a good cooperation and a pleasant experience. My friends, Robin Dahlbäck and Johanna Hanning, have together with rest of the staff at the Terahertz and Millimetre Wave Laboratory at Chalmers and Omnisys Instruments made sure that it is fun coming to work every day.

I also want to recognise my friends and family for all that that you have done for me. In particular, I would like to thank my parents Elisabeth and Göran. Thank you for everything and for always believing in me! Finally, I would like to thank my beloved girlfriend and companion Nicole. Although we have not been together for a very long time, you have already given me lots of encouragement and you have helped me make the right decision more than once. Thank you!

iv

List of publications

Appended papers

The following papers constitute the main work for this thesis:

[A]   **A. Hammar**, M. Whale, P. Forsberg, A. Murk, A. Emrich and J. Stake, "Optical Tolerance Analysis of the Multi-Beam Limb Viewing Instrument STEAMR," *IEEE Transactions on Terahertz Science and Technology,* vol. 4, no 6, November 2014

[B]   **A. Hammar**, Y. Karandikar, P. Forsberg, A. Emrich and J. Stake, "A 340 GHz High Gaussicity Smooth Spline Horn Antenna for the STEAMR Instrument," *IEEE International Symposium on Antennas and Propagation and USNC-URSI Radio Science Meeting*, Memphis, USA, July 2014

Other papers

The following papers are not included since the content overlaps or is beyond the scope of this thesis:

[a] **A. Hammar**, S. Cherednichenko, S. Bevilacqua, V. Drakinskiy and J. Stake, "Terahertz Direct Detection in $YBa_2Cu_3O_7$ Microbolometers," *IEEE Transactions on Terahertz Science and Technology,* vol. 1, no. 2, pp. 390-394, November 2011

[b] S. Cherednichenko, **A. Hammar**, S. Bevilacqua, V. Drakinskiy, J. Stake and A. Kalabukhov, "A Room Temperature Bolometer for Terahertz Coherent and Incoherent Detection," *IEEE Transactions on Terahertz Science and Technology,*, vol. 1, no. 2, pp. 395-402, November 2011

[c] **A. Hammar**, P. Sobis, V. Drakinskiy, H. Zhao, A. Emrich and J. Stake, "A 600 GHz Orthomode Transducer based on a Waveguide Integrated Wire Grid Polarizer," *23rd International Symposium on Space and Terahertz Technology*, Tokyo, Japan, April 2012

[d] **A. Hammar**, P. Forsberg, A. Emrich, M. Whale, A. Murk and J. Stake, "Optical Tolerance Analysis for the STEAMR Instrument," *24th International Symposium on Space and Terahertz Technology*, Groningen, the Netherlands, April 2013

Contents

Chapter 1

Introduction

In climate research, there is a growing interest for making observations of trace gases in the Upper Troposphere and Lower Stratosphere (UTLS). Studying the distribution of gases such as H_2O, O_3 and CO in the UTLS is an important task since the chemical composition and heat radiation processes taking place in this region affect the climate and therefore the living conditions on Earth [1]. These gas molecules have numerous resonant vibrational and rotational modes in the terahertz (THz) regime (100 GHz - 10 THz) and can be detected using sensitive receiving instruments [2]. There is a need to use these instruments for making measurements with high spatial resolution in order to provide input data for atmospheric models, which in turn can be used to improve climate change predictions and weather forecasts.

PREMIER[1] is the name of a satellite-borne mission with the aim of providing climate researches with the needed high spatial resolution measurement data in the UTLS. One of the two suggested instruments onboard the satellite is the Stratosphere-Troposphere Exchange And climate Monitor Radiometer (STEAMR), which is a 340 GHz limb-viewing radiometer observing the atmosphere at 14 different altitudes simultaneously. Figure 1.1 shows the nadir-looking instrument MetOp [4] working in synergy with STEAMR to, for example, estimate the amount of emissions from various anthropogenic and natural sources that can affect the climate.
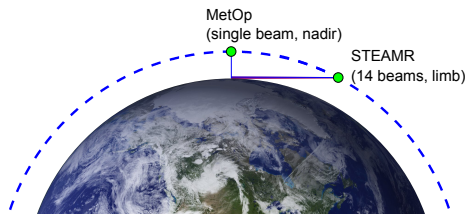

Figure 1.1: Illustration of STEAMR and MetOp in orbit 800 km above the Earth's surface.

---

[1]STEAMR is a Swedish contribution to PREMIER, which was one of three candidates for ESA's seventh Earth Explorer Mission [3]. Since it was not selected, a Swedish-Canadian collaboration was initated with the goal of making STEAMR part of a new mission called AliSS.

STEAMR has strong heritage from the Odin satellite [5] which is a single beam radiometer used both for aeronomy and radio astronomy. By utilising 14 beams simultaneously, STEAMR offers increased spatial and temporal resolution [6] over single beam instruments such as MLS [7, 8], MAS [9], Odin [5] and SMILES [10], which have to wobble up and down to cover the same region of the atmosphere, cf. figure 1.2. Besides the multibeam operation, STEAMR has several advantages over these instruments for measurements in the UTLS. Compared to MAS, MLS and SMILES, STEAMR has a higher resolution in the elevation direction provided by its primary reflector antenna measuring 1.6 m × 0.8 m, cf. figure 1.3. Odin achieves a high spatial resolution by using a 1.1 m circular antenna at frequencies up to approximately 600 GHz. However, atmospheric absorption at these frequencies is significant which makes a multibeam concept at 340 GHz more advantageous.

Figure 1.2: Wobbling single beam instrument (left) versus multibeam instrument (right).

When using several beams to observe the atmosphere, it is crucial to have a detailed knowledge on the performance of the optical system [12]. This requirement comes from the interpretation of the data measured by STEAMR, which is used for atmospheric models that use so-called retrieval functions [11] to establish a connection between the radiation from the atmoshpere to the signal being detected by the instrument.
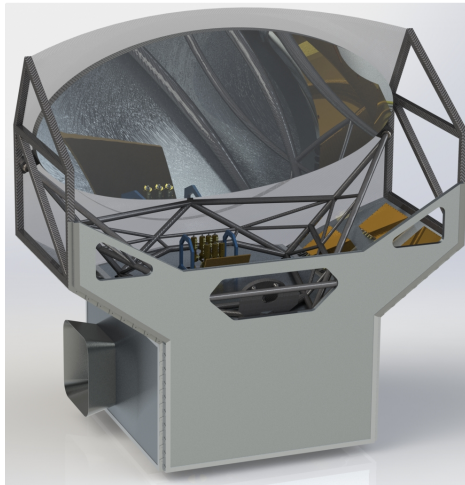

Figure 1.3: Mechanical CAD model of the STEAMR instrument

Compared to counterparts being used for visible light, optical systems at THz frequencies are typically much smaller compared to the wavelength (0.03 - 3 mm) and are therefore

noticably affected by diffraction. However, unlike the low-directivity antennas used for radio waves, reflector antennas for THz normally aim to produce a fairly collimated, albeit expanding, beam of radiation. The so-called Gaussian beam modes, originally developed for analysis of laser cavities [13, 14], are extensively employed to analyse reflector optics for THz (commonly referred to as quasi-optics). Simulation software for THz reflector antenna systems have developed alongside with the computing power of regular desktop CPUs and has thereby enabled the possibility to predict system performance to a degree that before was unattainable. These numerical methods are utilised in paper A, where the sensitivity to mechanical errors of the highly advanced optical system of STEAMR is investigated in order to have good input to the aforementioned retrieval functions.

Besides precise computer modelling, the success of optical systems for THz depends on good methods for manufacturing and electromagnetic as well as mechanical verification measurements. This requires a reliable test setup where the demands for accuracy in both electronics and mechanics are high. In paper B, the design and measurements of a smooth spline horn antenna for STEAMR is presented. The setup and test methods for this work are discussed thoroughly in this thesis.

Radiation in the THz regime, where STEAMR operates is non-ionising, but can penetrate many materials with relatively low losses. Despite this fact, there was for a long time little development of THz technology due to the difficulty of making practical and cheap devices such as powerful sources and sensitive detectors. This is about to change and applications are now found in fields such as atmospheric research [5, 15], security [16, 17], medicine [18], non-invasive inspection [19] and short-distance high-speed communication links [20]. However, applications for astronomy [21–25] have historically been the main driver for developing technology at THz frequencies [26]. A few examples of such instruments are shown in figure 1.4.
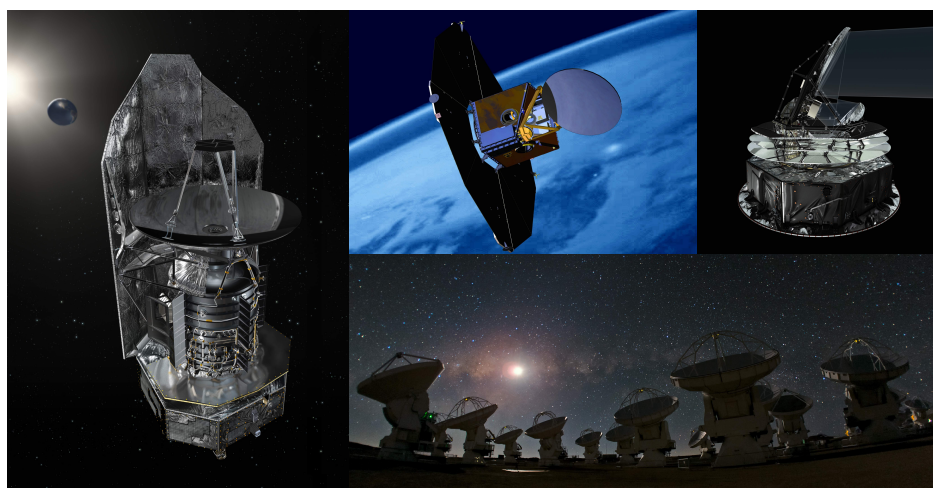

Figure 1.4: Instruments for astronomy and/or climate research operating at THz frequencies: Herschel Space Observatory [27], Odin [28], Planck [29] and Atacama Large Millimeter Array (ALMA) [30].

For the design of future such optical systems working in the THz regime, it becomes increasingly important for the designer to have an overlap in knowledge from different areas of science and engineering. Incorporating mechanical design and testing, combining different kinds of mathematical methods for analysis, electromagnetic antenna measurements and a firm understanding of optical requirements from the user are examples of considerations to take into account in order to achieve a well performing system to a reasonable cost. Thus, in order to be able to produce advanced optical systems for the THz domain, it is important to combine a scientific approach with industrial methods. It is the aim of this thesis to lay the foundation for such a line of action for future work on STEAMR and similar instruments.

Thesis outline

In chapter 2 of this thesis, radiometer receivers are introduced with extra attention given to the antenna system. Common types of reflector antennas and feeds are discussed along with analytical and numerical methods for analysis. Special attention is given to the Gaussian beam modes. Measurement techniques for characterising directive antennas are also presented. Chapter 3 summarises the STEAMR instrument with emphasis on the optical system. Results from optical tolerances and feed horn antenna measurements are shown and analysed. Concluding remarks of this work and a future outlook are given in chapter 4. Chapter 5 contains a short summary of the appended papers which this thesis are based upon.

Chapter 2

Antennas for radiometer systems

This chapter aims to describe the basics of radiometers as well as introducing reflector antenna systems. Important figures of merit for aperture antennas in radiometers are also presented. Gaussian beam mode analysis and its application for designing quasi-optical beam waveguiding systems is described in some detail. Some of the most important numerical methods for analysis of reflector antenna systems are briefly introduced. Finally, important measurement techniques are discussed.

2.1   Overview of radiometer systems

A microwave radiometer is a device for measuring the power of an incoming electromagnetic wave over a certain frequency bandwidth. It is a form of passive receiver and is therefore different from an active system (e.g. active radar) wherein the object under observation is illuminated by the transceiver and the scattered radiation is detected. Applications are often found in remote sensing of the Earth's atmosphere or radio astronomy where the thermal radiation being picked up typically constitute a weak and broadband signal, unlike the relatively strong and narrowband signals that are generated by active microwave sources.

The quantity specifying the amount of power dP of a source, which passes through a surface $d\sigma$ over a frequency span df' within a solid angle $d\Omega$ for a specified direction θ (angle between the surface normal and observation direction vector) is called the specific intensity (or spectral brightness) and it can be written as [31]

$$B_{f'} = \frac{dP}{\cos\theta \, df' d\sigma \, d\Omega} \quad [\text{W} \cdot \text{m}^{-2} \cdot \text{Hz}^{-1} \cdot \text{sr}^{-1}]. \tag{2.1}$$

Integrating the spectral brightness over the angle subtended by the source yields the flux density $S_{f'}$

$$S_{f'} = \iint\limits_{source} B_{f'}(\theta, \phi)d\Omega \quad [\text{W} \cdot \text{m}^{-2} \cdot \text{Hz}^{-1}], \tag{2.2}$$

which is the fundamental entity intercepted by the radiometer's antenna. In radio astronomy where signals are usually very weak, it is customary to work in units of Jansky (1 Jy = $10^{-26}\text{m}^{-2}\cdot\text{Hz}^{-1}$).

In applications for radio astronomy and Earth observations, it is customary to describe the incoming electromagnetic power in terms of an equivalent temperature. All physical objects having a temperature above absolute zero will emit electromagnetic radiation. An ideal black body will emit radiation according to Planck's law,

$$B_{f'}(T, \lambda) = \frac{2hf'^3}{c^2} \frac{1}{e^{\frac{hf'}{k_B T}} - 1} \quad [\text{W} \cdot \text{m}^{-2} \cdot \text{Hz}^{-1} \cdot \text{sr}^{-1}], \tag{2.3}$$

where h is the Planck constant, c the speed of light in the working medium, k_B the Boltzmann constant and T the physical temperature of the black body. In the Rayleigh-Jeans approximation it is assumed that $hf' \ll k_B T$ and a Taylor expansion can be used to re-write equation 2.3 as

$$B_{f'}(T) \simeq \frac{2f'^2 k_B T}{c^2} = \frac{2k_B T}{\lambda^2} \quad [\text{W} \cdot \text{m}^{-2} \cdot \text{Hz}^{-1} \cdot \text{sr}^{-1}] \tag{2.4}$$

This approximation is accurate for frequencies below 1000 GHz; cf. Figure 2.1.
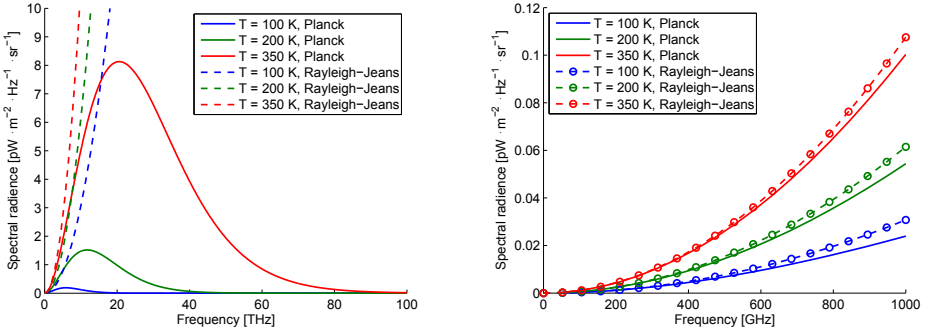
Figure 2.1: Comparison of spectral radiance as calculated using Planck's law and the Rayleigh-Jeans approximation at 100, 200 and 350 K.

Real sources have spectra that differ from the ideal Planck distribution. Such an object is referred to as a grey body and has an equivalent temperature T_B assigned to it in order to match the observed spectral brightness to an equivalent black body. The emissivity ϵ relates the brightness temperature to the physical temperature T:

$$T_B(\theta, \phi) = \epsilon(\theta, \phi)T. \tag{2.5}$$

It should be noted that the emmissivity for a general black body is also a function of frequency. The equivalent temperature T_B can now be used to define the antenna temperature T_A according to [32]

$$T_A = \frac{\int\limits_0^{2\pi}\int\limits_0^{\pi} T_B(\theta,\phi)G(\theta,\phi)\sin\theta d\theta d\phi}{\int\limits_0^{2\pi}\int\limits_0^{\pi} G(\theta,\phi)\sin\theta d\theta d\phi},$$ (2.6)

where $G(\theta,\phi)$ is the gain of the antenna, cf. equation 2.21.

The effective aperture of an antenna is defined by

$$A_e = \frac{P_A}{W_i},$$ (2.7)

where W_i is the power density of the incoming wave and P_A is the power delivered to the antenna. If a linearly polarised antenna receives radiation from a grey body with unpolarised light, half of the power delivered to the load is lost:

$$P_A = \frac{A_e W_i}{2}$$ (2.8)

Integrating equation 2.4 over frequency f' and the solid angle Ω subtended by the source gives the incoming power of the radiation:

$$W_i = \int\limits_{f_0'}^{f_1'}\iint\limits_{source} B_{f'}(T)G(\theta,\phi)d\Omega df' = \int\limits_{f_0'}^{f_1'}\iint\limits_{source} \frac{2k_B T(\theta,\phi)G(\theta,\phi)}{\lambda^2}d\Omega df'$$ (2.9)

Assuming an extended object at a constant temperature, and that the emissivity equals unity, it follows from equations 2.5 and 2.6 that $T = T_A$. Thus, equation 2.9 can be re-written as

$$W_i = \frac{2k_B T_A B}{\lambda^2}\iint\limits_{source} G(\theta,\phi)d\Omega = \frac{2k_B T B}{\lambda^2}\Omega,$$ (2.10)

where $B = f_1' - f_2'$ denotes the system bandwidth. Inserting this into equation 2.8 gives

$$P_A = \frac{A_e k_B T_A B\Omega}{\lambda^2}.$$ (2.11)

Using the antenna theorem [6, 33], which states that $A_e\Omega = \lambda^2$ for a single radiating mode, the following result is obtained:

$$P_A = k_B B T_A,$$ (2.12)

There is also an intrinsic noise contribution T_N from the radiometer itelf which is added to the antenna temperature [34]:

$$P_A = k_B B(T_A + T_N) = kBT_{sys},$$ (2.13)

where T_{sys} denotes the system noise.

For an ideal receiver with zero gain drifts, the sensitivity ΔT (in K), defined as the standard deviation of the output signal [34], is given by

$$\Delta T = \frac{T_{sys}}{\sqrt{B\tau}}, \tag{2.14}$$

where τ is the integration time. According to equation 2.14, the sensitivity approaches zero as the integration time becomes infinite. However, for any real system there are long-term gain drifts which must be included and therefore equation 2.14 is extended to include the RMS gain drift ΔG

$$\Delta T = T_{sys} \sqrt{\frac{1}{\sqrt{B\tau}} + \left(\frac{\Delta G(\tau)}{G}\right)^2}. \tag{2.15}$$

Figure 2.2 illustrates how the sensitivity can vary as a function of time based on the analytical expression above. This type of curve is often referred to as the Allan variance [35] and it can be used to find the optimum integration time of a radiometer. Instruments used for astronomy looking at cold objects can detect power variations in the order of a few millionths of one Kelvin [36]. In such applications, the system noise is often dominated by the receiver noise T_N. The situation is quite different for Earth observation, where the source can be several hundreds of Kelvin and therefore T_A has a larger impact on the system noise.
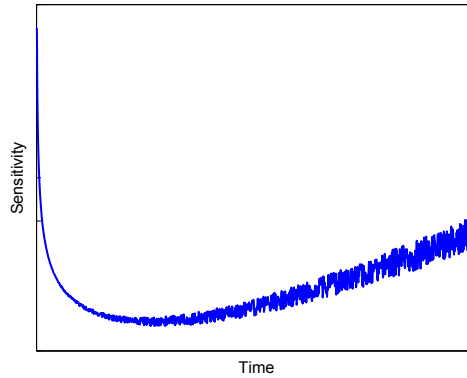
Figure 2.2: Allan variance curve showing how the sensitivity of a typical receiver varies as a function of the integration time.

There are two main detection schemes for radiometer systems, heterodyne detection and direct detection. The former uses a local oscillator (LO) signal to down convert the RF signal to a lower detectable frequency whereas a direct detector measures power in a well defined frequency band and converts the power into a corresponding DC signal. The content of this thesis will focus on heterodyne systems and direct detectors are not discussed. A heterodyne radiometer system can be divided into different sub-systems as shown in figure 2.3.

Most radiometer systems used for astronomy and Earth observation utilise a primary reflector antenna as a link between the source and the instrument. Following the primary reflector is one or several reflectors (and/or lenses) to couple the signal into a feed antenna. Due to

the system gain drifts discussed above, radiometer systems need to be calibrated against one or several known sources, which usually consists of thermal loads at a well known temperatures.
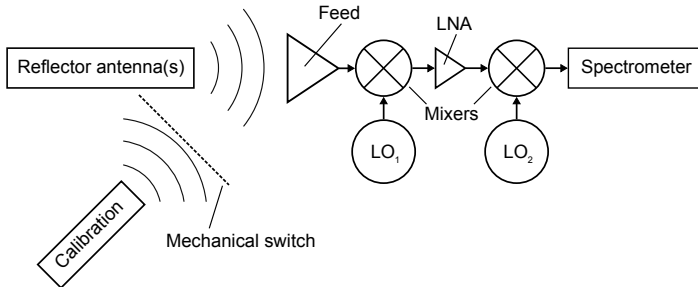

Figure 2.3: Simplified radiometer schematic. A mechanical switch that enables selection between observation the signal from the reflector antennas and the thermal calibration loads is indicated.

A mixer (or a low noise amplifier (LNA)) is often the first active component in the system following the antenna. Typically, it is the most significant contributor to system noise and the type of mixer being is used depends on the observation frequency. Cooled mixers have better noise performance, but require complicated and bulky cryogenic systems to work. SIS mixers are often used for systems operating below 1 THz [37, 38] whereas hot electron bolometer (HEB) mixers dominate for higher frequencies [39, 40]. Schottky mixers can be operated both with and without active cooling in the THz regime, from 100 GHz up to several THz [41–43]. However, the noise performance can not compare to SIS and HEB at high frequencies.

The LO system feeding the mixer needs to be carefully designed to deliver a stable signal with a minimised phase noise. Different phase-locking schemes are normally used to achieve a high quality LO signal. After being mixed down to an intermediate frequency (IF), the signal is typically amplified using one or several LNA stages before being sent to the backend. Depending on the frequency there might be further down conversion in the backend. At the final stage, the signal is analysed spectrally using a spectrometer, e.g. an FFT spectrometer, an autocorrelator or a chirp transform spectrometer.

2.2   Figures of merit for antennas

An antenna can be thought of as a device that takes electromagnetic radiation from free space into a guided wave structure. Due to the reciprocity theorem [32], the opposite also holds, i.e. antennas can convert a signal from a circuit into a propagating wave of electromagnetic radiation in free space. This means that antennas can be analysed in either transmit or receive mode depending on what is more suitable.

Knowing the size and the operating frequency of an antenna, it is possible to divide the space around it into three regions where the radiation pattern (i.e. radiated/transmitted power as a function of direction) varies significantly. These regions are referred to as the reactive near-field, the radiating near-field and the far-field of the antenna. For an antenna with largest

dimension D operating at a wavelength λ ($< D$), the distance r from the antenna is used to define the three regions as [32]

$$
\begin{aligned}
\text{Reactive near-field:} && 0.62\sqrt{D^3/\lambda} &< r \\
\text{Radiative near-field (Frensel diffraction):} && 0.62\sqrt{D^3/\lambda} &< r < 2D^2/\lambda \\
\text{Far-field (Fraunhofer diffraction):} && 2D^2/\lambda &> r
\end{aligned}
\tag{2.16}
$$

Even though there are no sharp transitions in the radiation pattern between the different regions, there are clear differences between the three regions. Close to the antenna the reactive part of the field dominates. In the radiative near-field, the radiation fields dominate and the radiation pattern varies as a function of r. In the far-field, the radiation pattern is no longer a function of r and the field components are perpendicular to the direction of propagation.

Beamwidth and side lobes

In studying the radiation pattern of an antenna it is useful to introduce the beamwidth as a parameter that immediatly reveals its main features. Beamwidth is here defined as the angular separation where the amplitude in the antenna pattern is equal on both sides of a maximum. This is illustrated in figure 2.4. The full width half maximum (FWHM) is the beamwidth of the main lobe where the power has dropped by a factor of $\frac{1}{2}$ from the maximum. For a uniformly illuminated antenna of size D, the FWHM (in radians) can be estimated using the following expression

$$
\theta_{FWHM} = 1.2217\frac{\lambda}{D}.
\tag{2.17}
$$

Taking into account the edge taper $T_{e,dB}$ for a Gaussian illuminated reflector[1], the FWHM can be estimated by [13]

$$
\theta_{FWHM,Gaussian} = (1.02 + 0.0135T_{e,dB})\frac{\lambda}{D}.
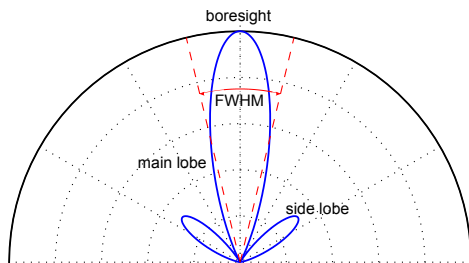\tag{2.18}
$$

Figure 2.4: Illustration of a radiation pattern in two dimensions with a main lobe and two side lobes.

Apart from the main lobe, any real antenna will have additional maxima in the radiation pattern which are referred to as side lobes, cf. figure 2.4. These are generally unwanted

---

[1]Gaussian beams and edge tapers are discussed in section 2.4

and consequently minimised in the antenna design. For a radiometer observing a target at boresight, a side lobe pointing in some other direction will add to the overall uncertainty of the measurement. The larger the difference in brightness between the boresight and side lobe direction, the larger the error in the measurement.

Gain and directivity

The directivity of an antenna is a function that specifies the radiation intensity (power per unit solid angle) as a function of direction in space. By definition, the directivity is a dimensionless quantity which is written as [32]

$$D(\theta, \phi) = \frac{U(\theta, \phi)}{U_0}, \tag{2.19}$$

where U is the radiation intensity and U_0 the radiation intensity of an ideal isotropic source. The maximum directivity D_{max} of a circular aperture is fundamentally limited by the aperture diameter D [32],

$$D_{max} = \left(\frac{\pi D}{\lambda}\right)^2. \tag{2.20}$$

Any practical antenna will suffer from ohmic losses due its finite conductivity and impedance mismatch losses on the input port. Collecting all such losses into an efficiency term called radiation efficiency, η_{rad}, one can write the antenna gain G as

$$G(\theta, \phi) = \eta_{rad} D(\theta, \phi). \tag{2.21}$$

The radiation efficiency is simply the ratio of total radiated power to the total input power of an antenna.

Similarly to the directivity, the antenna gain is defined as the radiation intensity of the antenna in a given direction normalised to the power accepted from the antenna if the source is radiating isotropically.

The power coupling ratio between two antennas in the far field is given by Friis transmission formula [44]

$$\frac{P_r}{P_t} = \eta_t \eta_r \frac{\lambda^2 D_t(\theta_t, \phi_t) D_r(\theta_r, \phi_r)}{(4\pi r)^2}, \tag{2.22}$$

where the subscripts t and r denote transmission and reception, respectively. The variables η_t and η_r represent the antenna efficiencies.

Aperture efficiency

The effective area A_e introduced in section 2.1 can be related to the physical area of the aperture A_p by the aperture efficiency η_a:

$$\eta_a = A_e/A_p \tag{2.23}$$

With an incoming plane wave $E_{t,pw}$ at the antenna aperture truncated at a radius r and with a field E_a from the antenna, the aperture efficiency can be written as [13]

$$\eta_a = \left[\frac{\iint E_a^* E_{t,pw} dS}{\iint E_a^* E_a dS \ \iint E_{t,pw}^* E_{t,pw} dS} \right]^2 \tag{2.24}$$

The aperture efficiency is always less than 1 and will ultimately limit the maximum achievable directivity. Thus, taking the aperture efficiency into account, equation 2.20 is modified to

$$D_{max} = \eta_a \left(\frac{\pi D}{\lambda} \right)^2 . \tag{2.25}$$

This is in part due to the fact that the feed antenna used to illuminate the reflector will have a radiation pattern that also illuminates the space next to the antenna. The fraction of power from the feed (cf Section 2.3.2) which does not intercept the antenna is referred to as spillover and the associated efficiency factor is called the spillover efficiency, η_s. Thus, spillover efficiency can be written as

$$\eta_s = \frac{P_{\text{intercepted}}}{P_{\text{feed}}} \tag{2.26}$$

The second factor making $\eta_a < 1$ is the so-called taper efficiency, denoted η_t (also known as illumination efficiency) which takes into account the non-uniformity of the incoming plane wave over the antenna aperture. There is a fundamental trade-off between spillover efficiency and taper efficiency which will determine the aperture efficiency, which is the product of the two; cf. Figure 2.5. For each application, the edge taper has to be chosen in order to obtain the best trade-off between taper efficiency and spillover efficiency. The optimal trade-off is not always the one resulting in a maximised aperture efficiency. For atmospheric research, it is common to have a high spillover efficiency to minimise side lobes that can be directed towards a hot source (e.g. the ground) and thereby decreasing the signal-to-noise ratio. Telescopes for radio astronomy do not normally have the same problem and are therefore optimised for maximum gain, which corresponds to an edge taper of 10.91 dB.
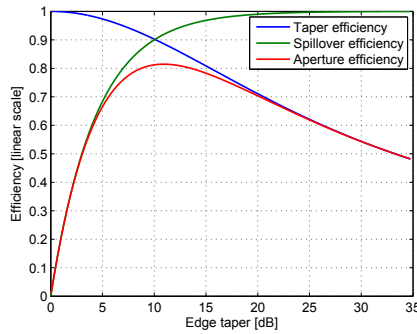

Figure 2.5: Taper, spillover and aperture efficiency as a function of edge taper.

Beam efficiency

As mentioned above it is often of high importance to minimise side lobes in radiometer systems. Interlinked with side lobe levels is another figure of merit known as the beam efficiency η_{BE}. It is defined as the ratio of power received/transmitted by an antenna within a cone angle θ_1 to the total power received/transmitted by the same antenna [32]. Mathematically, this can be expressed as

$$\eta_{BE} = \frac{\int\limits_0^{2\pi}\int\limits_0^{\theta_1} U(\theta,\phi)\sin\theta d\theta d\phi}{\int\limits_0^{2\pi}\int\limits_0^{\pi} U(\theta,\phi)\sin\theta d\theta d\phi}, \tag{2.27}$$

where U is the radiation intensity. The cone angle θ_1 has to be chosen appropriately for each application. One common choice is to choose the first nulls measured from boresight in order to only include the power in the main lobe. In some cases it can be difficult to clearly distinguish the side lobes and it is then customary to choose θ_1 as being equal to $2.5 \cdot \theta_{FWHM}$ [45], where again θ_{FWHM} is the angle representing the full width half maximum in the antenna radiation pattern.

Polarisation

Every antenna transmits/receives signals with a certain polarisation, i.e. direction of the E-vector as observed along the axis of propagation. Linear polarisation means that the polarisation vector does not change direction as the wave propagates, whereas elliptical (or in the special case circular) polarisation can be thought of as two E-vectors having a phase lag which results in an electric field vector that rotates about the axis of propagation. In any link between a target (e.g. another antenna or a signal stemming from some natural source), there will be an associated efficiency factor called polarisation efficiency. Mathematically, it is defined as [32]

$$\eta_{pol} = \frac{|\mathbf{l_e} \cdot \mathbf{E_i}|^2}{|\mathbf{l_e}|^2 \, |\mathbf{E_i}|^2}, \tag{2.28}$$

where $\mathbf{l_e}$ and $\mathbf{E_i}$ denote the vector that represents the polarisation characeristics of the antenna and the incident electric field, respectively.

2.3 Reflector antenna systems

Conic sections

One commonly used class of reflector antenna surfaces are the so-called conic sections, which are obtained by taking the intersection of a cone and a plane and creating a solid of revolution by rotating the curve about the symmetry axis. Spheroids, paraboloids, ellipsoids and hyperboloids can be obtained this way. Each type of conic section has two focal points and if a point source is placed in either, a perfect image (imaginary for the hyperbola) will be formed in the other. In the case of a circle the focal points coincide, whereas one of focal

point is infinitely far away for the parabola. The focal points for the ellipse and hyperbola are symmetrically distributed about the minor axis.

Having the vertex of the surface located in the origin of a Cartesian coordinate system, all conic sections can be described by the following expression

$$x^2 = 2R_{cs} - (K + 1)z^2, \tag{2.29}$$

where R_{cs} represents the on axis radius of curvature. K is often referred to as the conic constant and its value determine which curve is obtained. It is related the eccentricity e by

$$K = -e^2 \tag{2.30}$$

Table 2.1 shows a summary over the conic sections with important parameters.

Table 2.1: Conic sections with conic constants K, eccentricity e, semiminor axis b and equation expressed in terms of the half-foci distance c and half-vertex separation a in a Cartesian frame.

Conic section	K	e	b	Equation
Oblate ellipse	> 0	c/a	$\sqrt{a^2 - c^2}$	$(z/a)^2 + (x/b)^2 = 1$
Circle	0	0	a	$z^2 + x^2 = a^2$
Prolate ellipse	$> -1, < 0$	c/a	$\sqrt{a^2 - c^2}$	$(z/a)^2 + (x/b)^2 = 1$
Parabola	-1	1	∞	$z^2 = 4ax$
Hyperbola	< -1	c/a	$\sqrt{c^2 - a^2}$	$(z/a)^2 - (x/b)^2 = 1$

Alternatively, the conic sections can be defined by a set of three numbers r_1, r_2 and θ_i. For an axial ray emanating from one focus, r_1 and r_2 represent the distances from the the foci to the reflection point on the optical element. If a focal point is behind the reflector surface, the corresponding distance (r_1 or r_2) is defined to be negative. θ_i is the angle between the axial ray and the normal of the surface with $0 \le \theta_i \le \pi/4$.

Figure 2.6: Parabola
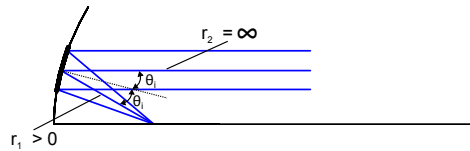
2.3.1   Telescopes

A telescope in this context is a device for collection light and image formation. It normally consists of one or several reflectors (and/or lenses) designed to match a feed antenna or a beam waveguide optically. Here, a distinction is made between reflectors of the telescope and the reflectors of a beam waveguide. It is the telescope that ultimately defines the imaging
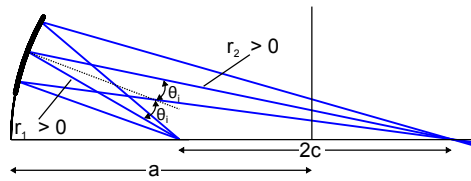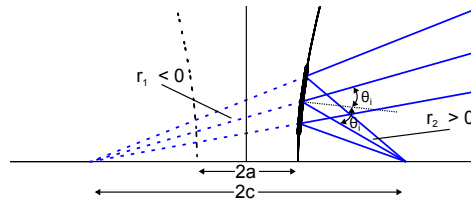
Figure 2.7: Ellipse

Figure 2.8: Hyperbola

quality of the system and its field of view, whereas a beam waveguide consisting of a series of reflectors has the purpose to shape the beam in order to match it to the feed antenna.

Early telescope designs date back to the 17th century and theoretical work of Mersenne, Decartes, Herschel, Gregory and Cassegrain [46]. The Gregorian and Cassegrainian designs are classic 2-mirror telescopes that were suggested at the time, cf. figure 2.9. Both telescopes have a parabolic primary reflector. The main difference between the two is that an intermediate focus is formed between the primary and ellipsoidal sub reflector of the Gregorian design, whereas the Cassegrainian design has no intermediate focus and employs an hyperboloid surface for the sub reflector. For a ground based radiometer system, the two reflector system is often preferable to a prime focus telescope (cf. figure 2.6) since any spillover from the feed antenna will radiate towards the sky instead of the significantly warmer ground.
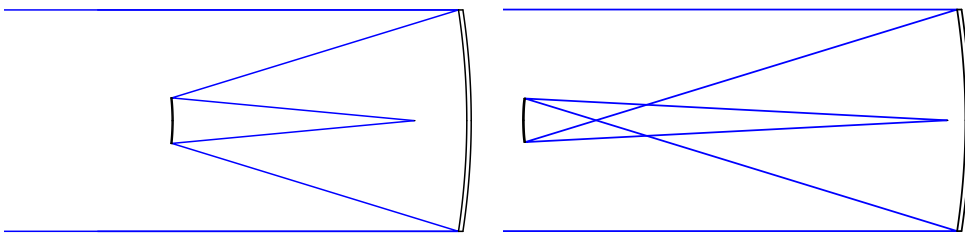

Figure 2.9: Cassegrainian (left) and Gregorian (right) designs.

Spherical aberration[2] was addressed and minimised for in these designs. However, difficulties in manufacturing reflectors with correct shape hindered the scientists to realise the

---

[2]Aberrations are discussed in section 2.5

systems at the time. Newton was the first to actually manufacture a reflective telescope. His telescope utilised a flat reflector making a 45° to the optical axis to re-direct the light from the parabolic reflector to an observer outside the telescope tube, cf. Figure 2.10. Up until today, limitations in manufacturing ultimately sets the boundary for optical performance.
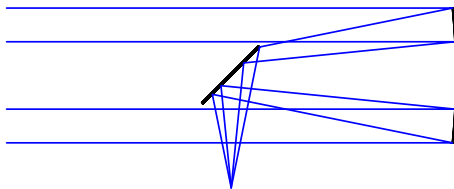

Figure 2.10: Newton telescope

It was not until 1927, when Ritchey built the first reflective so-called aplanatic telescope, correcting both for spherical aberration and coma (or comatic aberration), that a real advance was made in terms of optical quality. The theoretical groundwork was laid by Schwarzhild and Chrétien [46] a few years earlier which lead to the name Ritchey-Chrétien telescope. This telescope is a modification of the classic Cassegrain design where the parabolic primary reflector is replaced by a hyperbolic surface that is co-optimised with the hyperbolic sub-reflector to produce an image free of third-order coma and spherical aberration. Equivalent aplanatic telescopes can also be made in the Gregorian form using ellipsoidal surfaces for both the primary and sub reflector. The effects of coma worsen with increasing field angles and is therefore the main limiting aberration of field of view for the classic telescopes. Notable examples of Ritchey-Chrétien designs are The Hubble Space Telescope [47], the Very Large Telescope (VLT) [48] and Herschel Herschel Space Observatory [22]. Planck is an example of an instrument using an aplanatic Gregorian telescope [23].

Figure 2.11 shows an example of an off-axis reflecting telescope. The main motivation for choosing off-axis portions of the reflector parent bodies is to minimise diffraction from the subreflector and its support structure caused by blockage of the main beam. Off-axis designs are usually preferred in place of simply tilting the reflectors since the latter option causes additional aberrations. More advanced designs involve tilted off-axis reflectors as well as a tertiary reflector to minimise all Seidel aberrations [49]. Employing an off-axis design may introduce cross polarisation due to the unsymmetric currents on the surface. However, by letting the design fulfill the so-called Dragone-Mizugutchi condition [50, 51], cross polarisation can be elliminated.
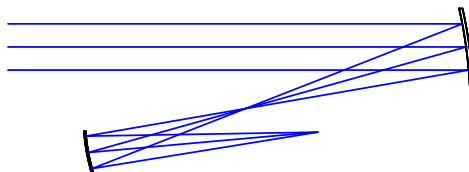

Figure 2.11: Off-axis Gregorian telesope

The f/D or f-number constitute one of the most important parameters for any optical system. In the geometrical optics limit ($\lambda = 0$), f/D is defined as the ratio of the system effective focal length to the entrance pupil diameter D [52]. However, in the microwave/quasi-optical approach, the f/D is usually defined as the ratio of the focal length of the primary aperture to its diameter. As pointed out in section 2.2, D also has a direct impact on the size of a beam from a diffraction dominated reflector antenna. In an optical system dominated by aberrations, D can be thought of a parameter that determines the amount of light that can be collected.

2.3.2 Antenna feeds

Any reflector antenna system has a feed antenna matching the impedance of free space to that of the receiver. At frequencies above 1 THz, it is common to use printed lens-integrated antennas [39], whereas circularly symmetric feed horns are more common at lower frequencies. Physically, a feed horn antenna is a hollow metal structure that is tapered down from the aperture to the waveguide connection of the receiver. Some examples of designs that have been used over the years are pyramidal, E-plane, H-plane, conical and exponential horns [53]. To a large extent such geometries can be analysed by analytical means to predict important performance parameters such as side lobe levels, Gaussicity[3], cross polarisation and beamwidth.

Increased computing power and advances in computational electromagnetics software using mode-matching, finite differences time domain (FDTD) and finite element method (FEM) [54] etc. have enabled short simulation times and the capability to resolve minute details in the radiation power. In fact, the biggest uncertainty in feed horn synthesis of today comes from imperfections in manufacturing. Three important types of feed horn antennas, namely the Potter, spline and corrugated horns, are described in terms of basic geometry and performance below. These are all examples rotationally symmetric horns which have been designed to minimise side lobe levels and cross polarisation while having a highly symmetrical main beam.

Potter horn

A Potter horn antenna [55] (also known as dual mode horn) is circularly symmetric and consists of piecewise linearly tapered sections, cf. figure 2.12. In designing this type of horn, both dominant modes of a circularly symmetric waveguide, i.e. the TE_{11} and TM_{11}, are excited and appropriately balanced in phase and amplitude to achieve a highly symmetrical main beam with side lobes at levels 30 dB below the maximum. Gaussicity and cross polar levels of the Potter horn are approximately 96.3% and 1.4% [56]. Moreover, a Potter horn has a 10% bandwidth in terms of -20 dB cross polarisation level.

Having a profile radius that is monotonically increasing, the Potter horn is relatively easy to fabricate with good precision and is hence a sufficient option as a feed for many reflector antenna systems.

---

[3]Gaussicity refers to the coupling to the fundamental Gaussian beam mode; cf. section 2.4.
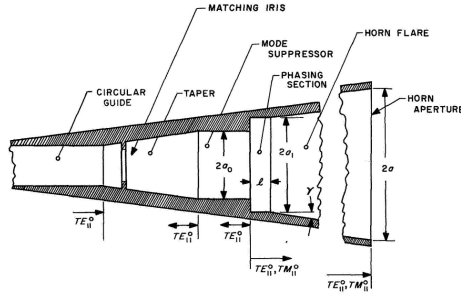
Figure 2.12: Potter horn [55].

Corrugated horn

By superimposing circularly symmetric grooves to a smooth conical horn, a corrugeted horn (also called scalar horn) antenna can be obtained. For the most basic design of a such an antenna, the depth of the corrugations are increased from $\lambda/2$ at the back of the horn, referred to commonly as the throat section, and then readily tapered to $\lambda/4$ which is then maintained as far as the aperture, cf. figure 2.13. Having a groove depth of $\lambda/4$ will cause the ϕ components (in cylindrical coordinates) of the E and H fields to have infinite reactances and hence, $E_\phi = H_\phi = 0$. This gives the so-called balanced hybrid mode condition which results in a highly uniform field distribution across the aperture, which in turn gives low side lobes, axial symmetry of the beam and high Gaussicity (98.1%). Bandwidths in cross-polar and side lobe levels of $20 - 40\%$ can be obtained. For these reasons, the corrugated horn has been used extensively over the years for radio telescopes. Several alternative designs for corrugated horns have been made. For instance, horn designs which are made with corrugated spline profiles and analysed using higher order HE_{1n} modes, have demonstrated Gaussicities of $\sim 99.8\%$ or more over a limited bandwidth [57].
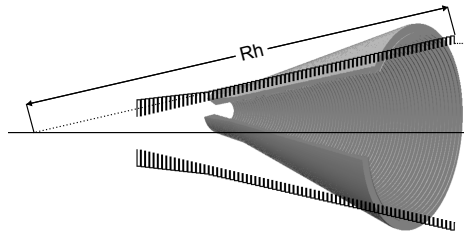
Figure 2.13: CAD model of a corrugated horn with opening on the side. The profile of the horn is superimposed in black.

Manufacturing corrugated feed horns poses a major challenge compared to the smooth profile designs like the Potter horn. If the corrugations are large (i.e. the frequency is low enough) standard lathing methods may be used. However, as the frequencies of interest increase, the features inside the horn become more difficult to manufacture and hence more

expensive. One common method is to fabricate a mandrel having the shape of the corrugated horn, which is then used as a "negative" in a electroplating process where metal is grown to form the horn [58]. The mandrel is dissolved in the final step to lay bare the horn. This method has proven to work, but is highly complicated, time consuming and therefore expensive. Other methods for manufacturing corrugated horns include precision milling in metallic split-blocks or stacking metallic ring-shaped shims of varying inner diameter to define the desired corrugated profile shape [59]. These fabrication methods will however limit the performance due to mechanical deviations which become larger in comparison to the wavelength as the freqcuency is increased.

It is possible to predict the size and position of the Gaussian beam waist using the following design equations [13]:

$$w_o = \frac{0.644a}{1 + [\pi(0.644a)^2/(\lambda R_h)]^2} \tag{2.31}$$

$$z = \frac{R_h}{1 + [\lambda R_h/(\pi(0.644a)^2)]^2} \tag{2.32}$$

Here a is the aperture radius of the feed and R_h is the slant length from the aperture to the center of curvature, cf. figure 2.13.

Spline horn

Even though scalar feed antennas have excellent performance in terms of many important figures of merit, the manufacturing process becomes a serious issue at THz frequencies due to the fine details in the interior of the horns. For instance, at 300 GHz, the desired depth of the corrugations ($\lambda/4$) is 0.25 mm. Granet et. al. [60] have shown that a smooth horn profile having an optimised, non-linear taper can give similar or better performance of the corrugated feed horn. This is achieved at the cost of having a feed that is approximately 50% longer than the corrugated one, cf. figure 2.14. In contrast to the Potter horn, a non-linear profile taper is allowed and therefore more degrees of freedom are obtained.
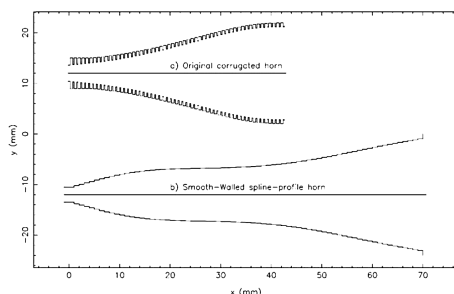

Figure 2.14: Corrugated horn (a) and spline horn (b) at 80-120 GHz with similar performance. Taken from [60].

Analysis of the spline horn is made using mode-matching software that divides the feed horn into small segments and calculates scattering parameters for a large number of propagat-

ing modes. The field distribution in the horn aperture is finally calculated and used to obtain the far-field radiation pattern. Side lobe levels at 35 dB below the maximum can be obtained with a Gaussicity of $> 98\%$. The performance in terms of bandwidth of a spline horn can be up to 50%, depending on its length. The aforementioned major advantage to the corrugated horn has to do with the manufacturing process, which is much simpler.

2.4 Gaussian beam modes

This section describes the Gaussian beam mode analysis and it builds largely upon the material which can be found in [13, 14, 61]. Gaussian beam modes represent a set solutions of Maxwell's equations that describe a propagating beam of radiation that is fairly collimated, i.e. it has some variation perpendicular to the axis of propagation in contrast to a plane wave which is constant in the transverse direction.

As described in section 2.3.2, many feed horns have radiation patterns with high Gaussicity and Gaussian beams can be evaluated analytically at any point in space. Hence, the Gaussian beam modes consist a simple and practical tool for analysing a wide range of optical systems in the sub-mm region.

In free space in the absence of free charges and with an electric field $\mathbf{E}$ varying in time as $e^{-i\omega t}$, Maxwell's equations reduce to the Helmholtz equation:

$$\left(\nabla^2 + k^2\right)\mathbf{E} = 0, \tag{2.33}$$

where the wave number k is equal to $2\pi/\lambda$. Just as for a plane wave it is assumed that the electric and magnetic fields are mutually perpendicular and perpendicular to the axis of propgation which is here chosen to be the z axis. Neglecting time dependence, the ansatz

$$E(x, y, z) = u(x, y, z)\exp(-ikz) \tag{2.34}$$

can be inserted into equation 2.33 to yield the reduced wave equation:

$$\frac{\partial^2 u}{\partial x^2} + \frac{\partial^2 u}{\partial y^2} + \frac{\partial^2 u}{\partial z^2} - 2ik\frac{\partial u}{\partial z} = 0 \tag{2.35}$$

By assuming that the variation of the amplitude of u along the z axis is small over a distance similar to one wavelength and that the axial variation will be small compared to the variation transverse to z, the third term in equation 2.35 can be neglected:

$$\frac{\partial^2 u}{\partial x^2} + \frac{\partial^2 u}{\partial y^2} - 2ik\frac{\partial u}{\partial z} = 0 \tag{2.36}$$

Equation 2.36 is known as the paraxial wave equation, which in cylindrical coordinates becomes

$$\frac{\partial^2 u}{\partial r^2} + \frac{1}{r}\frac{\partial u}{\partial r} - 2ik\frac{\partial u}{\partial z} = 0, \tag{2.37}$$

where axial symmetry, i.e. $\frac{\partial u}{\partial \varphi} = 0$, is assumed for the so-called fundamental Gaussian beam mode. For higher order Gaussian beam modes this assumption is not made.

The normalised solution for equation 2.37 may be written as

$$E(r, z) = \left(\frac{2}{\pi w^2}\right)^{0.5} \exp\left(\frac{-r^2}{w^2} - ikz - \frac{i\pi r^2}{\lambda R} + i\phi_0\right) \tag{2.38}$$

The parameter w is called the beam width and corresponds to the beam radius where the amplitude of the E-field has dropped by a factor of $1/e$ from its maximum value. R is the radius of curvature of the equiphase surface. As can be seen in figure 2.15, w attains a minimum value referred to as the beam waist w_0. ϕ_0 is called the Gaussian beam phase shift or Gouy phase shift. Equations 2.39, 2.40 and 2.41 can be used to express w, R and ϕ_0 as a function of z, w_0 and λ:

$$R = z + \frac{1}{z}\left(\frac{\pi w_0^2}{\lambda}\right)^2 \tag{2.39}$$

$$w = w_0\left[1 + \left(\frac{\lambda z}{\pi w_0^2}\right)^2\right]^{0.5} \tag{2.40}$$

$$\phi_0 = \arctan\left(\frac{\lambda z}{\pi w_0^2}\right) \tag{2.41}$$

Making use of the so-called confocal distance, defined as

$$z_c = \frac{\pi w_0^2}{\lambda}, \tag{2.42}$$

equations 2.39, 2.40 and 2.41 can conveniently be expressed as

$$R = z + \frac{z_c^2}{z} \tag{2.43}$$

$$w = w_0\left[1 + \left(\frac{z}{w_c}\right)^2\right]^{0.5} \tag{2.44}$$

$$\phi_0 = \arctan\left(\frac{z}{z_c}\right) \tag{2.45}$$

Using Gaussian beam modes requires that the beam waist radius satisfies

$$w_0 \geq 0.9\lambda \tag{2.46}$$

in order to give accurate results [62]. Below 0.9λ the accuracy degrades gradually and comes to a complete failure at approximately 0.2λ or less.

When designing a quasi-optical system it is vital to know the fraction of the total energy in the beam which is intercepted by an element of a given size. The edge taper is T_e is defined as the fraction of power at a radius r compared to the on-axis power:

$$T_e = \frac{P(r)}{P(0)} = \exp\left[-2\left(\frac{r}{w}\right)^2\right] \tag{2.47}$$

Figure 2.16 shows how the power of the fundamental Gaussian beam mode intercepted by a circular aperture varies as a function of radius normalised to the beam waist. The half power is intercepted at a radius of 0.6 w_0. For a radius of w_0 and $2w_0$, the intercepted power is 86% and 99.97%, respectively. The edge taper is often expressed in logaritmic scale given by

$$T_{e,dB} = -10\log_{10}(T_e). \tag{2.48}$$

Relating the edge taper (in logarithmic scale) to r and w gives the following equation:

$$T_{e,dB} = \left(\frac{r}{0.3393w}\right)^2 \tag{2.49}$$
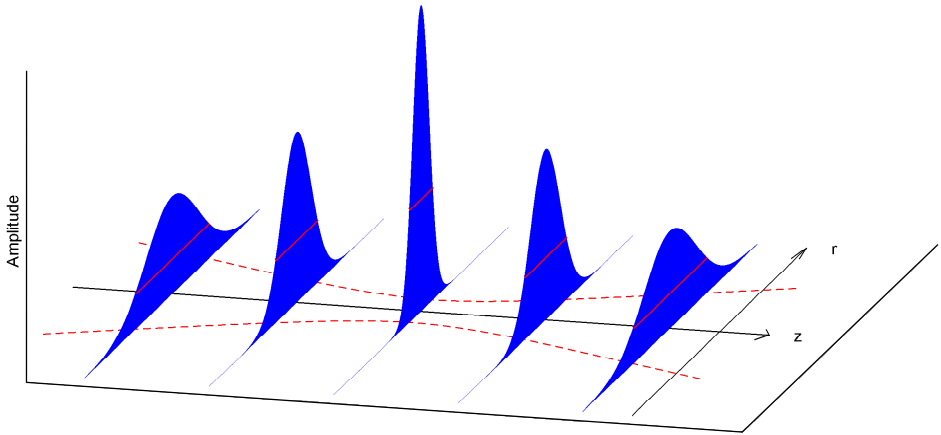

Figure 2.15: Illustration of a propagating Gaussian beam. The $1/e$ level of the electric field is highlighted in red.
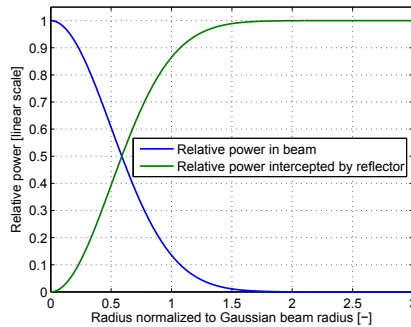

Figure 2.16: Fractional power of a fundamental Gaussian beam mode intercepted by an optical element of a certain radius.

There is a simple way to describe a quasi-optical system consisting of an arbitrary number of optical elements using cascading matrices, where the only input parameters are the focal lengths of the elements and the intermutual distances. For these purposes it is convenient to to re-write equation 2.38 as:

$$E(r, z) = A(z) \exp \left[\frac{-ikr^2}{2q(z)} \right] \exp(-ikz) \tag{2.50}$$

In this expression, the function $q(z)$ is called the complex beam parameter and it can be expressed as:

$$q(z) = \left(\frac{1}{R} - \frac{i\lambda}{\pi w^2} \right)^{-1} \tag{2.51}$$

Being a function of R, λ and w, $q(z)$ contains a complete description of the fundamental Gaussian beam mode. For a given $q(z)$, the beam width, radius of curvature and Gouy phase shift can be obtained by using the formulas given in the following equtions:

$$w(z) = \left[\frac{\lambda}{\pi \mathrm{Im}(-1/q(z))} \right]^{0.5} \tag{2.52}$$

$$R(z) = \left[\mathrm{Re} \left(\frac{1}{q(z)} \right) \right]^{-1} \tag{2.53}$$

$$\phi_0(z) = \arctan \left[\frac{\mathrm{Re}(q(z))}{\mathrm{Im}(q(z))} \right] \tag{2.54}$$

A system with a certain number of optical elements can be described by a 2×2 matrix M_n called the ray transfer matrix, which in turn is composed by the product of ray transformation matrices. Each such matrix represent either an optical element or a distance. The elements of the ray transfer matrix are denoted A, B, C and D:

$$\begin{bmatrix} A & B \\ C & D \end{bmatrix} = \prod M_n \tag{2.55}$$

The basic ray transformation matrices are given in equations 2.56 and 2.57. These desribe transformation of $q(z)$ by propagation of a distance z and phase transformation by a thin lens (or reflector) with focal length f, respectively.

$$M_{\text{propagation}} = \begin{bmatrix} 1 & z \\ 0 & 1 \end{bmatrix} \tag{2.56}$$

$$M_{\text{thin lens}} = \begin{bmatrix} 1 & 0 \\ -1/f & 1 \end{bmatrix} \tag{2.57}$$

Starting with an initial $q(z) = q_{in}$, the resulting complex beam parameter q_{out} after transformation of by the ray transfer matrix is described by equation 2.58.

$$q_{out} = \frac{Aq_{in} + B}{Cq_{in} + D} \tag{2.58}$$

A first-order design of a beam waveguide system can be obtained using the techniques discussed above. In many practical cases it is enough to only consider the fundamental Gaussian mode. This is indeed sufficient for many practical reflector systems where the coupling to the fundamental Gaussian mode η_G (Gaussicity) is well above 90%. Mathematically, this coupling is given by

$$\eta_G = \left[\frac{\iint E_a^* E_G dS}{\iint E_a^* E_a dS \; \iint E_G^* E_G dS} \right]^2, \tag{2.59}$$

where E_G denotes the field for the fundamental Gaussian beam mode. Having only one single main lobe, with no side lobes and zero cross-polarisation, the fundamental Gaussian beam represents a highly desirable radiation pattern.

For a general conic section off-axis reflector, the focal length f is found by

$$f = \left(\frac{1}{r_1} + \frac{1}{r_2} \right)^{-1}, \tag{2.60}$$

where r_1 and r_2 are the distances experienced by a ray emanating from one focal point and being imaged in the second via a reflection in the reflector surface, cf. figures 2.6, 2.7 and 2.8. Equation 2.60 is valid for a point source and therefore have to be modified to be applicable for Gaussian beams which have a source of finite extent. The following expression describes the field from a scalar point source

$$u_p = \frac{e^{-jkR_p}}{R_p}, \tag{2.61}$$

where R_p is the distance from the source to the field point. In Cartesian coordinates, R_p is equal to $\sqrt{x^2 + y^2 + z^2}$. For a circularly symmetric beam propagating along the z axis R_p can be written as

$$R_p = \sqrt{\rho^2 + z^2}, \tag{2.62}$$

with $\rho^2 = x^2 + y^2$. If the point source is moved to a complex field point where z is replaced by $z + iz_c$ (z_c being the confocal distance as defined by equation 2.42) the expression in equation 2.62 can be written as

$$R_p = \sqrt{\rho^2 + (z + iz_c)^2} \approx z + iz_c + \frac{\rho^2(z + jz_c)}{2(z^2 + z_c^2)}, \tag{2.63}$$

where it is assumed that $z^2 + z_c^2 \gg \rho^2$ which holds in the paraxial limit. Inserting this into equation 2.61 yields

$$u_p = \frac{e^{-jkR_p}}{R_p} \propto \frac{1}{A'} \exp\left(\frac{-\rho^2}{A'^2} - \frac{ik\rho^2}{2B'} - ikz - C' \right), \tag{2.64}$$

where $A'^2 = \frac{2w_c}{k}\left(1 + (z/z_c)^2\right) = w_0^2\left(1 + (z/z_c)^2\right)$, $B' = z + z_c^2/z$ and $C' = \arctan(\frac{z}{z_c})$. Comparing with equations 2.43, 2.44 and 2.45 A', B' and C' can be identified with the beam width w, the radius of curvature R and Gouy phase shift ϕ_0, respectively. By also comparing the expressions given in equation 2.38 and 2.64, it is clear that a Gaussian beam may be described

as a point source having an imaginary offset equal to the confocal distance z_c in the direction of propagation. Therefore, for a fundamental Gaussian beam, equation 2.60 can be re-written as

$$f = \left(\frac{1}{r_1 + iz_{c_1}} + \frac{1}{r_2 + iz_{c_2}} \right)^{-1}, \tag{2.65}$$

where z_{c_1} and z_{c_2} are the confocal distance for incoming and reflected beam, respectively. Taking the real part of equation 2.65 and comparing with equation 2.43 gives

$$f = \left(\frac{1}{z_1 + \frac{z_{c_1}^2}{z_1}} + \frac{1}{z_2 + \frac{z_{c_2}^2}{z_2}} \right)^{-1} = \left(\frac{1}{R_1} + \frac{1}{R_2} \right)^{-1}, \tag{2.66}$$

where R_1 and R_2 represent the radius of curvature for the beams prior to and after reflection, respectively. Thus, using these surfaces for Gaussian beams requires that the waist of the incoming beam is moved away from the focal point in order match the radius of curvature of the beam given by equation to the curvature of the optical surface.

2.5 Numerical methods for analysis of reflector antennas

Gaussian beam mode analysis can be used for generating a design for a reflector antenna system where the coupling to the fundamental Gaussian beam mode is high. However, the increase in computer power and the development of advanced simulation software in recent years have enabled antenna designers to predict the system performance to a degree that was not possible in the past. This section serves to give a brief description of the most relevant methods for designing reflector antenna systems. Basic concepts are explained and advantages and limitations of the different methods are discussed.

2.5.1 Ray tracing

Optical systems operating in the visible spectrum where the size of the optical elements typically are several orders of magnitude larger than the wavelength can to a large extent be designed and analysed using methods of ray tracing. Diffraction is not directly taken into account in this approximation as the wavelength is assumed to be zero and it follows that light behaves as rays traveling along straight lines unless the refractive index changes. Snell's law describes how a ray bends when crossing a surface that separates two media of refractive index n_1 and n_2:

$$n_1 \sin \theta_1 = n_2 \sin \theta_2 \tag{2.67}$$

Here, θ_1 and θ_2 denote the angle between the ray and the surface normal prior to and after refraction (reflection), respectively. For a reflector in air, $n_1 = -n_2 \simeq 1$.

The general goal for an optical system is to accept incoming light from an object and manipulate its wavefront (equi-phase surface) in order to create an image. Ideal imaging in terms of ray tracing is achieved when every ray of light emanating from a point in the object

plane is imaged to precisely one point in the image plane. Any real optical system is in fact always unable to do so and the errors are referred to as aberrations, which are divided into point aberrations and field aberrations [52]. The former makes the image blurry/unfocused whereas the latter distorts its shape.

There are different kinds of aberrations of which the so-called Seidel aberrations - spherical aberration, coma, astigmatism, field curvature and distortion [52] - are the most extensively studied when designing an optical system. The analysis is based on a third-order Taylor expansion of Snell's law. Higher order aberrations are sometimes considered depending on the requirements. First-order optics, or Gaussian optics[4], is used to find the focus point in the paraxial approximation. For a system that utilises one or several lenses, so-called chromatic aberrations are introduced due to the wavelength dependence on refractive index in every refractive medium.

Two of the Seidel aberrations, spherical aberration and coma are illustrated in figure 2.17. Spherical aberration occurs on-axis and transforms a flat wavefront in such a way that the focus is smeared out along the optical axis. A single spherical reflector will have spherical aberration, but this can readily be removed by employing a paraboloid surface instead, cf. section 2.3. Even if a paraboloid surfce is employed, incoming rays that are not parallel to the axis of the paraboloid will not be imaged to a single point. Instead, off-axis points will be imaged to a pattern that resembles a comet on the sky. This phenomenon is called coma and can be corrected (to third order) by introducing a secondary reflector in the optical system, cf. Section 2.3.1. Astigmatism can be thought of as an effect that gives two separated foci along the optical axis depending on which plane is considered. In a rotationally symmetric system third-order astigmatism occurs only for off-axis objects, wheras higher order astigmatism also occurs on-axis in systems lacking rotational symmetry. The latter kind of astigmatism can also be exploited as part of the design, cf. Section 3.1.

Figure 2.17: Lenses having spherical aberration (left) and coma (right) with corresponding spot diagrams. Note that the lens to the right also has some additional spherical aberration.

Zemax [63] and CODE V [64] are examples of software packagess that are extensively used by the industry and which both utilise ray tracing methods for analysis and optimisation of a wide range of optical systems. Due to the relative speed of ray tracing, a large number systems can be evaluated in a short space of time, e.g. when optimising or testing the sensitivity to mechanical errors. Analysing higher order aberrations analytically is extremely complex - a problem that is immediately overcome by ray tracing software that normally includes all higher order aberrations. Another commonly used software package is GRASP (General Reflector and Antenna Farm Analysis Software) [65]. Although it mainly used for solving reflector antenna problems using methods physical optics (PO) and physical theory of

---

[4]Note that this is different from the Gaussian beam modes discussed in section 2.4

diffraction (PTD), cf. section 2.5.2, it also contains built-in ray tracing routines. Two methods, simply called geometrical optics (GO) and geometrical theory of diffraction (GTD) are used for problems where the size of the reflectors are much greater than the wavelength. It is significantly faster than PO/PTD or any full wave method, but the results are only accurate in the far field. Moreover, GO/GTD also has the disadvantage of errors due to caustics, i.e. regions where all parallel rays in a bundle focus and where the intensity becomes infinite. The focal point of a paraboloid reflector is an example of such a point. This is seen in the far field pattern calculated by GO/GTD at $\theta = 0$, where a dip can be seen. However, different correction routines can be employed to counteract this problem.

2.5.2 Physical optics, physical theory of diffraction and method of moments

The material presented in this section is taken from the GRASP technical description [66]. GRASP is nowadays considered the standard tool for analysing reflector optics systems and it has been used for several optical simulations presented in this thesis. Calculations performed by the software rely on the aforementioned methods PO/PTD, GO/GTD and Method of Moments (MoM).

Combining PO and PTD is often the best trade-off between accuracy and calculation speed when analysing systems which are relatively large in comparison to the wavelength. The simulations described in chapter 3.1 all rely on this combination of methods. In the short wavelength limit PO and PTD calculations will become increasingly heavy. However, GO/GTD is genereally much faster and the calculations become increasingly accurate in this limit and may therefore be employed instead of PO and PTD.

Method of moments

One limitation of PO/PTD is that the order in which the scattered fields propagate between reflectors has to be determined a priori. This is not the case for MoM, which is a highly accurate method used to determine the scattered fields based on a full-wave solution of Maxwell's equations and, therefore, diffraction effects and multiple reflections are taken into account automatically. It is a good option for reflector optics systems where $D < 20\lambda$, but it has the disadvantage of lengthy calculations and high working memory requirements for structures that are large compared to the wavelength. Increasing the discretisation of the scattering surfaces corresponding to N unknowns makes the memory requirement grow as N^2. However, the discretisation used for MoM is only made on the scattering surfaces themselves. FEM on the other hand, has a working memory consumption that grows linearly with the number of unknowns, but the discretisation has to be made in the whole space of interest around the scatterer and thereby effectively making the memory requirement grow as N^3. Therefore, MoM is an appropriate method for open boundary problems for moderately sized scatterers where the required accuracy is high.

Physical optics

PO is a method where an incident field on a perfectly/partially conducting reflector induces surface currents which are used to calculate the scattered field. The total electric field $\mathbf{E}$ around a reflector is written as

$$\mathbf{E} = \mathbf{E}^i + \mathbf{E}^s, \tag{2.68}$$

where $\mathbf{E}^i$ and $\mathbf{E}^s$ denote the incident and scattered fields, respectively. The surface currents on a finite size curved reflector are calculated by dividing the reflector into several smaller parts where the currents on each part are approximated by the currents of a plane reflector of infinite size. The surface current $\mathbf{J}^e$ due to an incoming magnetic field $\mathbf{H}^i$ is given by

$$\mathbf{J}^e = 2\hat{\mathbf{n}} \times \mathbf{H}^i, \tag{2.69}$$

where $\hat{\mathbf{n}}$ is the surface normal unit vector. By numerically integrating over all surface currents, the electric and magnetic vector potentials $\mathbf{A}^e$ and $\mathbf{A}^m$ at an arbitrary point in space $\mathbf{r}$ can be calculated. These are then used to determine the actual electric and magnetic fields. In a system consisting of a series of consecutive reflectors, the calculated scattered field from a reflector is used as the incident field for the following reflector. The far fields can be calculated according to

$$\mathbf{E}(\mathbf{r})_{far} = \lim_{r \to \infty} \mathbf{E}(\mathbf{r}) kr \exp(ikr) \tag{2.70}$$

$$\mathbf{H}(\mathbf{r})_{far} = \lim_{r \to \infty} \mathbf{H}(\mathbf{r}) kr \exp(ikr), \tag{2.71}$$

where $r = |\mathbf{r}|$.

The accuracy of a PO calculation increases as the number of sample points grows but so does the computation time. To find a good trade-off, the user must specify a convergence limit for the calculated field and a convergence calculation can be used to find the appropriate number of sample points on the reflector surface.

The power in the fields calculated by PO is given by the Poynting vector:

$$\mathbf{P} = \frac{1}{2} \mathrm{Re}(\mathbf{E} \times \mathbf{H}^*), \tag{2.72}$$

where $\mathbf{H}^*$ denotes the complex conjugate of the magnetic field. This can be used to calculate the spillover by at each reflector. The fraction of the power which intercepts the reflector is found by integrating the power δW over an infinitesimal area δs, $\delta W = -\mathbf{P} \cdot \hat{\mathbf{n}} \delta s$ over the reflector surface B:

$$W = -\iint_B \mathbf{P}(\mathbf{r}') \cdot \mathbf{n}(\mathbf{r}') ds', \tag{2.73}$$

where $\mathbf{n}$ is the unit normal surface vector pointing out from the illuminated side of the surface. In logarithmic scale, the spillover is given by

$$\eta_{s,dB} = -10 \log_{10}\left(\frac{W}{4\pi}\right), \tag{2.74}$$

where the factor 4π indicates that the power is normalised to 4π W, which is the default power radiated by a feed in GRASP.

Physical theory of diffraction

As mentioned above, it is assumed in PO calculations that surface currents are calculated for a flat and infinetly large surface. This approximation does not hold near the edge of a reflector where PTD has to be employed. Instead of approximating the area around the sample point with an infinite plane, the PTD method models the surface near an edge as a semi-infinte surface, i.e. a surface extending to infinity in one direction. The electric field emanating from the PTD calculations are subsequently added to that of the PO calculation to get a better approximation of the total scattered field:

$$\mathbf{E}^s = \mathbf{E}^s_{\text{PO}} + \mathbf{E}^s_{\text{PTD}} \tag{2.75}$$

One limitation of PTD is that the incident field must resemble a plane wave near the edge of the reflector. Also, the PTD method starts to give inaccurate results as the beam truncation of the reflector increases. In such situations methods such as MoM may be a better choice.

The appropriate number of points to be used the current calculations in PO/PTD depends upon several factors such as the aperture size and the wavelength. Typically, the accuracy of the side lobe levels is worse for large off-axis angles. Setting a low convergence limit in GRASP is one simple way to automatically determine the number of points necessary for the calculations.

2.6 Measurement techniques

Characterisation of an antenna is a task that can be performed in many different ways depending on the antenna under test (AUT) and the objective of the measurement. Since antennas for microwave radiometers are typically dealing with fairly collimated beams of radiation, this section focuses solely on the measurement schemes developed for such directive antennas, and hence, methods for antennas that are more or less omni-directional are omitted. Special attention is given to the planar near field scanner working in a rectilinear frame.

Overview

Directly measuring the radiation pattern of an antenna is undoubtedly the ultimate way of characterisation, but such tests may in some cases also be completed by mechanical measurments in combination with electromagnetic simulations. Typically, it is the the goal to measure the far field radiation pattern of an antenna, and due to reciprocity, antennas can be measured in both receive and transmit mode with an incoming plane uniform wave being the ideal in the former case [32]. Measuring a feed horn which is in the order of 10λ can typically be made directly in the far field at THz frequencies. However, as can be seen from equation 2.16, probing a large reflector antenna in the far field may be challenging. For example, a 1 m reflector at 300 GHz has a far field that begins 2 km away from the aperture - a distance too large and a frequency too high even for the world's largest far field range [67].

It is therefore common to employ setups where the antenna is measured in the near field. In order to calculate the far field from the measured near field of the antenna it is then necessary to investigate spatial variation of the amplitude, phase and polarisation. Alternative

approaches where the amplitude only is sampled in several planes perpendicular to the antenna boresight are also sometimes used [68]. A probe antenna (outside the reactive near field) is normally used to couple radiation to the AUT for this purpose. Common types of probes include open-ended waveguides (rectangular or circular), corrugated horns and pyramidal horns. It is important that the radiation pattern of the probe does not have too large influence of the measurement, which means that the probe has to be chosen carefully for each application. The need to deconvolve the probe pattern in order to obtain the true radiation pattern from the AUT is typically larger when a directive feed horns is being used. Open-ended waveguide have nearly omni-directional radiation patterns and a probe pattern deconvulution is therefore not always necessary.

A basic scheme for the signal acquisition is shown in figure 2.18. Two phase-locked synthesizers are used to generate an RF signal and a reference signal (from "Synth$_1$" and "Synth$_2$" in figure 2.18, respectively) that are slightly offset in frequency. The RF signal feeds the AUT which radiates a field that is collected by the probe. The signal from the probe is down-converted using the reference signal. A well-controlled relative movement between the probe and the AUT changes the amplitude and phase from the received signal ("IF$_{RF}$" in figure 2.18). This signal is compared to the IF signal of the synthesizers to obtain the radiation pattern from the AUT.
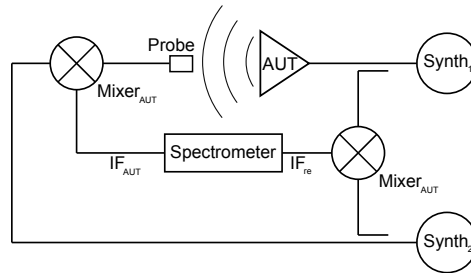

Figure 2.18: Basic scheme for a near field scanner.

Compact antenna test range and holograms

Figure 2.19 shows one commonly used test setup, the Compact Antenna Test Range (CATR). In this arrangement, one or several offset reflectors are used together with a feed to produce an approximately plane wavefront for illuminating the AUT and thereby emulating the far field condition. Finite sized reflectors having non-ideal shapes, direct illumination from the feed and reflections from the surrounding walls result in a confined usable space around the AUT known as the quiet zone. As can be seen in figure 2.19, the edges of the reflectors are serrated. The purpose of this is to make the transition from metal to free space "smoother" in order to minimise diffraction patterns in the quiet zone from the reflector edges.

A CATR is, despite its name, very spatious and the relatively high complexity of the system drives up the cost. An alternative method to generate a plane wave was presented in [70] where a microwave hologram was used. The 1.1 m dish of Odin was measured at

Figure 2.19: CATR setup located at ESTEC in Noordwijk, the Netherlands [69].

119 GHz using a 2.4 m × 2.0 m hologram [71], and more recent publications show results at 650 GHz [72]. One drawback of the hologram solution is that each hologram has to be tailor-made for a specific frequency.

Near field measurements

An alternative approach is offered by directly probing the phase and amplitude of the radiation pattern from the AUT in the near field. This can be done using several different schemes, whereof spherical, cylindrical and planar geometries are the most common.

In the spherical geometry, the AUT is rotated about θ for a set of fixed ϕ values. The situation is quite different for the cylindrical geometry where the probe is swept vertically (z direction) for a set of fixed azimuth values (i.e. rotations of the xy plane about the z axis). For a planar near field scanner, the field is most often sampled in rectilinear coordinates by sweeping the probe in a meander pattern, cf. figure 2.20. Other geometries such as plane-bipolar and plane-polar can also be used [68]. An open-ended waveguide probe is normally used since (as discussed above) its nearly omni-directional radiation pattern will not influence the coupling too strongly when displacing the probe relative to the AUT. However, corrections for the probe radiation pattern can be employed if the need precise measurements is more extreme.

Even though the basic principle is simple, near field measurements at THz frequencies imply several difficulties that have to be dealt with. The phase of the signal is generally
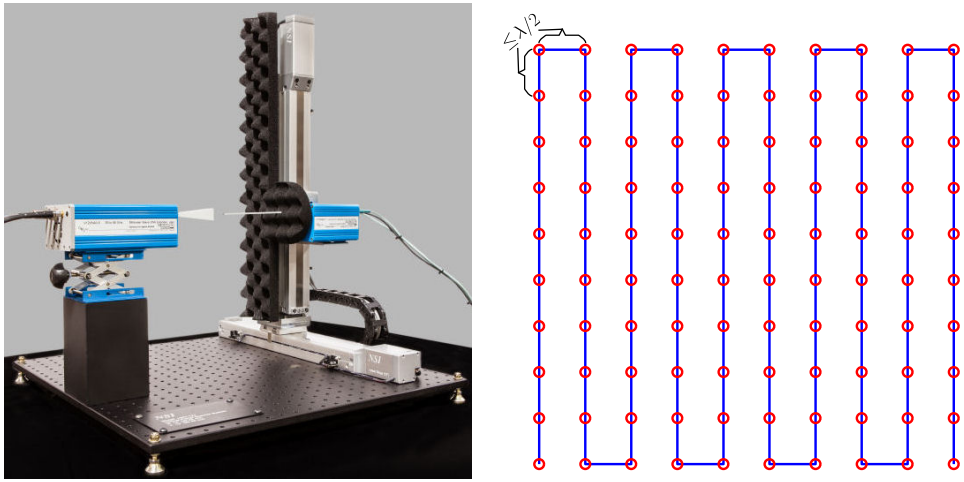
Figure 2.20: Compact near planar near field scanner taken from [73] (left) and meander pattern (blue line) illustrating the movement of the probe and the measurement points (red circles) (right).

the most difficult to measure accurately. Typically, there is a notable phase drift in the electronics when working at high frequencies. The additional movement of the probe may also introduces phase errors.

Scew movement of the linear stages causes the probe move in a plane that deviates from the ideal flat one. Because of the probe's nearly omni-directional radiation pattern, the probe-AUT coupling is not particularly sensitive to rotational misalignment of the probe when the co-polar pattern is being measured. However, the cross-polar pattern is significantly more sensitive to tilts about the boresight axis of the probe. Unwanted movement of the probe along the boresight direction of the AUT causes a phase error proportional to the deviation. Although highly unwanted, this error can be corrected given that the deviations of the scanner have been measured mechanically.

Vibrations due to the moving parts in the system will also have some effect on the phase errors. Commercial manufacturers of high-frequency systems have addressed this problem by employing a heavy base of granite to which the linear stages are firmly fixed [74]. Being a material with low thermal expansion, granite is also well suited for near field scanners where bending of the linear stages due to changed thermal conditions can cause phase errors that are difficult to control.

Coaxial cables will unavoidably bend as the probe moves during the measurement. When this happens, one side of the cable will be compressed whereas the other will be streched. This causes the characteristic impedance of the cable to change and this manifests itself as an additional change in relative phase that varies as a function of position of the probe. Changed thermal conditions will have a similar effect on the measured phase. This last problem can, to some extent, be avoided by matching cable lengths between from the synthesizers to make phase drifts cancel, cf. figure 2.18. Stabilising the temperature in the room where

the measurements are performed is the most obvious way of handling the problem. This also counteract phase drifts in active microwave components that will also affect the antenna characterisation.

Standing waves are another issue encountered when measuring an antenna in the near field. As can be seen in figures 2.19 and 2.20, specially shaped material is used to absorb and scatter the waves away from the probe. A good absorbing material typically has a return loss of -40 dB or better. As directive antennas are considered, the need for absorbing material is highest around the probe and AUT. In cases where this is not sufficient, rooms completely covered in absorbers, so-called anechoic chambers, may be used. To further reduce the standing waves, it is desirable to avoid perpendicular planar surfaces in the path between the probe and AUT. Hence, it is common to have chamfered edges on both AUT and probe to scatter radiation away from the probe. When lenses are being used it is common to use anti-reflection coatings for the same purpose.

In accordance with the Nyqvist sampling theorem, and as is indicated in figure 2.20, the sampling distances Δx and Δy (for a hypothetically infinite scan area) should be $\lambda/2$ to enable a full reconstruction of the radiation pattern in the far field [68]. When the maximum angle of coverage θ_{max} from boresight is less than $\pm 90°$, the criterion is modified to

$$\Delta x = \Delta y = \frac{\lambda}{2 \sin \theta_{max}}. \tag{2.76}$$

The inherenet truncation of a planar near field scanner affects the radiation pattern over the whole far field sphere, but a good measurement can be reliable to angles up to $\pm 80°$. Beyond that limit, spherical setups that do not suffer from the same truncation problems have to be used. It is worth noting that the purpose of all measurements is not to predict the far field. In some cases, it could be more interesting to compare the near field results to those predicted from simulations by evaluating the coupling integral.

Minimising the AUT-probe distance will allow for an increased θ_{max} for a given size of the planar near field scanner, which in turn increases the angular range where the far field is accurate. As mentioned above, it is important to keep the probe outside the reactive near field. A distance of 3λ to 5λ are often preferable.

Given a plane geometry of the scanner, a plane wave expansion of the measured field to obtain the far field radiation pattern is convenient. Using the tangential part of the angular spectrum $\mathbf{F}_T$

$$\mathbf{F}_T(k_x, k_y, z = 0) = \int_{-\infty}^{\infty} \int_{-\infty}^{\infty} \mathbf{E}_T(x, y, z = 0) e^{j(k_x x + k_y y)} dx dy, \tag{2.77}$$

where $\mathbf{E}_T(x, y, z = 0)$ is the measured field (tangential field components), k_x and k_y the wavenumbers projections in x and y, the electric field at an arbitrary position in space can be determined by [68]

$$\mathbf{E}_T(x, y, z) = \frac{1}{4\pi^2} \int_{-\infty}^{\infty} \int_{-\infty}^{\infty} \left(\mathbf{F}_T(k_x, k_y) - \hat{z} \frac{\mathbf{k} \cdot \mathbf{F}_T(k_x, k_y)}{k_z} \right) e^{-j\mathbf{k} \cdot \mathbf{r}} dk_x dk_y. \tag{2.78}$$

Chapter 3

STEAMR: Optical analysis and characterisation

3.1 System description

The Stratosphere-Troposphere Exchange And climate Monitor Radiometer (STEAMR) is an instrument for atmospheric research in the upper troposphere/lower stratosphere (UTLS). It was originally proposed for as part of the Process Exploration through Measurement of Infrared and millimeter-wave Emitted Radiation (PREMIER) mission [1], which was one of three candidates for ESA's seventh Earth Explorer Mission [3]. Since it was not selected, a Swedish-Canadian collaboration was initiated with the goal of making STEAMR part of the AliSS mission. The optical system [75–78] presented in this thesis is for the version of STEAMR which was proposed for the PREMIER mission. To study radiation from the UTLS is important in order to understand how the chemical composition of the atmosphere and the climate are connected. This knowledge in turn is key to understand the impact on the climate due to human activities.

STEAMR uses 14 beams for limb sounding observations of the atmosphere. Figure 3.1 shows the beam distribution of on the sky. Since high lateral sampling is prioritised, it is possible to use elliptical beams which have the minor axis aligned with the elevation direction on the sky. Consequently the primary aperture has an elliptical aperture of 1.6 m × 0.8 m, cf. figure 3.2. The object plane is located 3325 km away from the instrument and has a lateral coverage of 22 km with sampling density of 1.5 km at altitudes < 16.5 km and 2.0 km at higher altitudes. The multi-beam concept enables observations at 14 targets simultaneously, which is used for tomographic reconstruction of the chemical composition of the UTLS [11]. This may also be acheived with a single wobbling beam, but at the cost of decreased spatial/temporal resolution and therefore lower sensivity.

Sub-harmonically pumped Schottky mixer receivers [79, 80] are used to cover the frequency bands 323-335 and 343-355 GHz. A multiplier generated LO signal at ~175 GHz is used for down-conversion to intermediate frequencies (IF) ranging from 3.6-15.6 GHz.

Autocorrelators are used in the back-end to detect the IF signals with a 10 MHz resolution.
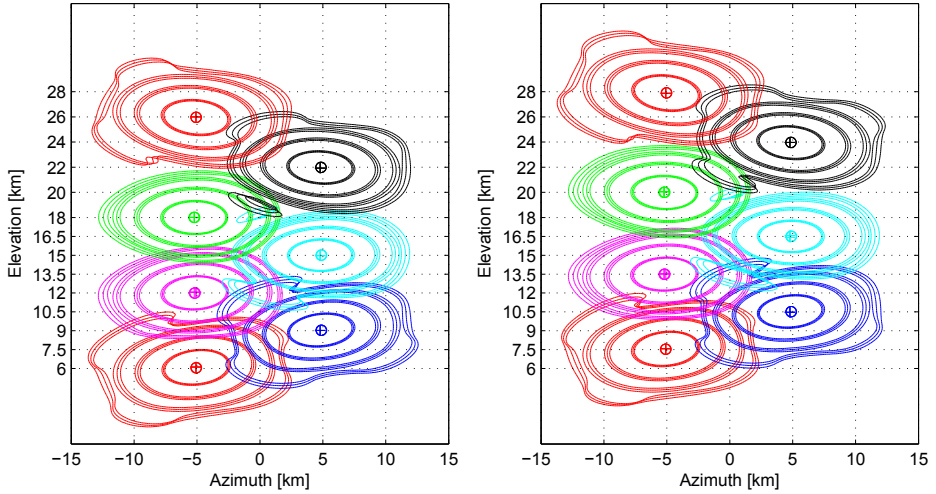

Figure 3.1: Simulated STEAMR beam layout on the sky [75]. Contours to the left correspond to beams having a polarisation plane $-45°$ to the orbital plane and the beams to the right correspond having a polarisation plane $45°$ to the orbital plane.

3.1.1   Optical system

The purpose of the optical system of STEAMR is to image and re-shape the 14 elliptical beams to circular to match the respective feed horns located in the focal plane array (FPA). Moreover, the imaging should be frequency independent, meaning that the illumination of the primary aperture should be same over the whole frequency band. Equation 2.18 shows that the FWHM of the main lobe will be a linear function of λ if the edge taper is constant. Combining equations 2.18, 2.40 and 2.49 gives

$$
\begin{aligned}
\theta_{FWHM,Gaussian} &= (1.02 + 0.0135 T_{e,dB})\frac{\lambda}{D} \\
&= \left[1.02 + 0.0135\left(\frac{r}{0.3393 w_0 \sqrt{1+\left(\frac{z}{w_c}\right)^2}}\right)^2\right]\frac{\lambda}{D}
\end{aligned}
\tag{3.1}
$$

Choosing $z = 0$ corresponds to placing the primary aperture at the waist, i.e. where $w = w_0$ and where the phase shift is 0 for the outgoing Gaussian beam. This is equivalent of having an overall phase shift between the feed horns and primary aperture of an integer multiple of π. Thus, the way that the STEAMR optical train works to minimise the frequency dependence is by ensuring an overall beam phase shift of an integer π and by matching the beam size to the primary aperture to obatain the desired edge taper of 25 dB. This edge taper is chosen to achieve a large beam efficiency, and thereby avoiding side lobes receiving signals from the relatively warm ground, rather than maximising the aperture efficiency, cf. section 2.2.

With a main aperture of 1.6 m in the lateral direction, the size of the FWHM beam contour in the image plane will differ by approximately 250 m at the outermost frequencies used by the instrument.

A total of six reflectors and two multi-faceted FPAs with $2 \times 2 \times 7$ reflector surfaces are used in the optical system. The reflectors in the optical system (denoted M1-M8), are separated into three different sub-systems referred to as the FPA, the relay optics and the telescope. These are all described below. A complete design for the calibration system optics was not made for the PREMIER version of the STEAMR optics and is therefore not included in this section.
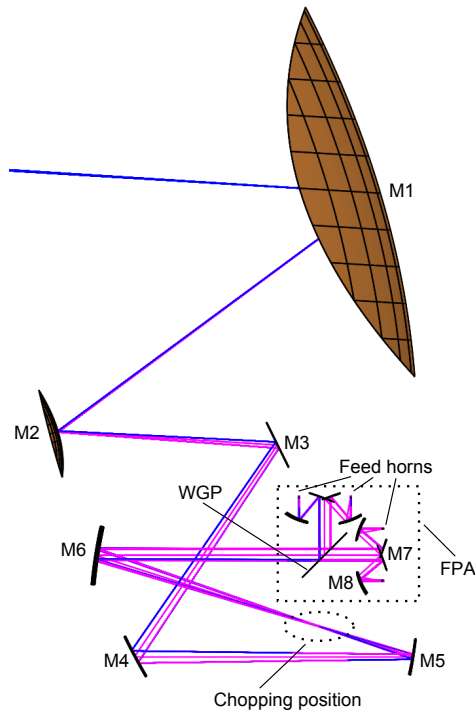

Figure 3.2: GRASP CAD model of the optical train of STEAMR. The optical system is symmetric in the plane of the picture.

Focal plane array

For its 14 receivers, STEAMR uses two sets of FPAs that are separated in polarisation by the use of a wiregrid polariser (WGP) to achieve polarisation interleaved beams in order to increase the vertical resolution, cf. figure 3.1. As is shown in figure 3.3 one FPA consists of metal structures with monolithically machined faceted surfaces and integrated feed horns to ensure good mutual alignment.
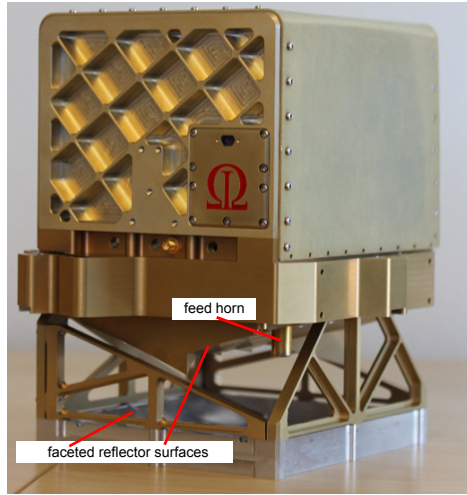
Figure 3.3: FPA prototype with faceted reflectors for 7 beams.

The output focal plane of the FPA is located at M7 and it is placed in such a way that the Gouy phase shift to the primary aperture is $(n - 0.5)\pi$, where $n \geq 1$ is an integer. In the PREMIER version of the STEAMR optics, $n = 2$, cf. figure 3.4. In the Gaussian beam picture, the focal plane is thus an image of the far field. The reason for this is that the phase shift from the beam waist at the primary aperture to the far field is $\pi/2$. Hence, the total phase shift between the focal plane and the far field is 2π. This is done in order to maximise the mutual separation of the beams on the sky and consequently in the FPA. Having a phase shift $\neq (n - 0.5)\pi$ means that the beam overlap in the FPA will increase, which leads to more truncation and consequently higher power losses and uncertainty in the radiometric measurements. The beam spacing requirements on the sky lead to an edge taper at the M7 reflector of 18.2 dB.

Relay optics

Following the FPA is the relay optics which consists of reflectors M6-M3. This is the part of the optical system where re-direction of the beams to the calibration sub-system and the circular to elliptical beam formation takes place.

Its first reflector (M6) intercepts the 14 parallel beams from the FPA and bring them to a point where they overlap, cf. figure 3.2. At this point, a chopper reflector mounted on a shaft will steer thee beams towards a thermal load in each calibration cycle.

To shape the beams, three reflectors (M5-M3) work together in a network [75] consisting of astigmatic reflectors [81] that have different focal lengths in the xz (azimuth) and yz (elevation) plane. To ensure high power throughput all reflectors in the relay optics have an edge taper of 40 dB corresponding to a relative loss of 0.1‰ at each reflector.
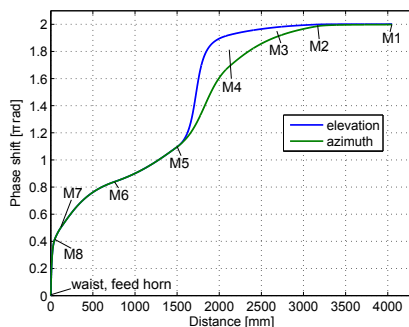
Figure 3.4: Gouy phase shift for a Gaussian beam propagating from the feed horn to the primary aperture. The on-axis distance for all reflector positions are highlighted (M8-M1). The phase shift between the M5 and M2 reflectors differs as a result of the beam forming network that treats the elevation and azimuth directions as two separate sets of propagating Gaussian beams.

Telescope

The M1 and M2 reflectors constitute the telescope which serves to image the beams from the relay optics to the targets on the sky. In contrast to the FPA and the relay optics, the telescope was initially desiged using ray-tracing methods to obtain a rotationally symmetric Ritchey-Chrétien telescope with off-axis cut-outs. As mentioned in chapter 2.3.1, this telescope design not only corrects for spherical aberration but also for third order coma which makes it a suitable choice for a multi-beam instrument with a large field of view. Edge tapers for the telescope are 40 dB and 25 dB for the M2 and M1 reflectors, respectively. Using equation 2.18, the FWHM for the 1.6 m × 0.8 m is calculated to be 0.043° or, equivalently, 2.49 km on the sky, in the elevation direction at 340 GHz.

3.2 Mechanical tolerances

For advanced optical systems, such as photographic objectives or microscopes, investigating the sensitivity to mechanical deviations must be part of a successful design. The acceptable deviations are referred to as tolerances. Due to the high number of optical components, each having six degrees of freedom (three translation, three rotation), the number of possible combinations of perturbations for such optical systems is vast. For a simpler system consisting of one or two optical elements, scenarios such as worst-case, expected etc. can be simulated with relative ease. For more advanced optical systems, statistical methods (e.g. Monte-Carlo [82]) are often more practical.

In the short-wavelength limit where ray tracing is used, thousands of systems can be evaluated relatively fast to generate statistic distributions to show the expected spread in performance after manufacturing with given mechanical tolerances. However, for an advanced optical system like STEAMR operating in the sub-mm regime, more computationally heavy methods such as PO/PTD are usually employed. This complicates the tolerance analysis
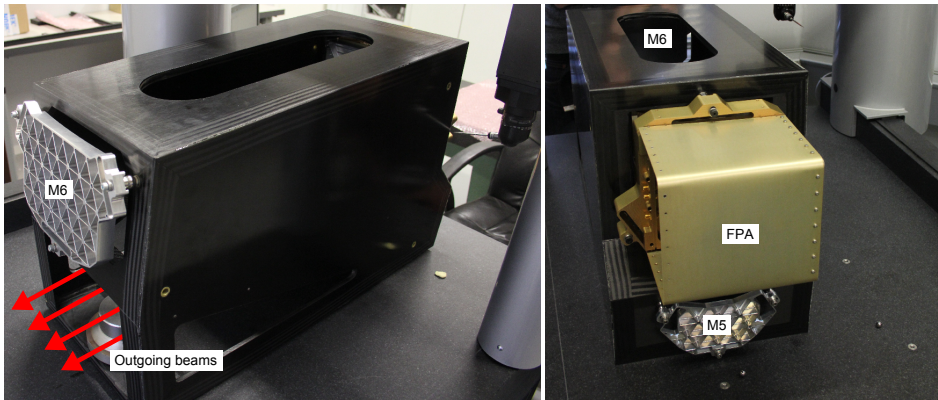
Figure 3.5: Photos showing demonstrator during alignment measurements using a CMM.

which has to be simplified in order to make the simulation times reasonable. This problem is addressed in paper A, where a methodology was used in which simulations for relative beam pointing and worst-case beam distortion were separated using ray tracing and PO/PTD in Zemax and GRASP, respectively. By doing so, a large number of systems could be tested with respect to relative beam pointing, which is the most outstanding problem in terms of in-orbit stability and is thus used as the primary metric in establishing performance of the system. Thus, the actual optical requirements were factored in to ease the calculation load instead of investigating all possibilities.

The methodology also included the manufacturing of a demonstrator, cf. figure 3.5 which also enabled simplifications to be made in the tolerance analysis. For instance, it was shown that the FPA unit could be manufactured with a high degree of conformity and this part was consequently assumed to be ideal as other types of errors could reasonably be expected to dominate. Preliminary results from the tolerance analysis were also used when manufacturing the demonstrator. This way of using concurrent engineering proved to be an efficient way to work for the industry when developing sub-mm optics.

3.3   Prototyping and antenna measurements

3.3.1   Measurement setup

To fully characterise reflector antenna systems and feed horns, a setup for measuring phase and amplitude was developed. A planar scanner was used to determine the fields from reflectors and to measure the Gaussicity of feed horns, cf. figure 3.6.

As shown in figure 3.7, two phase-locked synthesizers with YIG oscillators were used to generate signals at ~14 GHz. Following power splitters on both sides are cascaded Schottky diode multiplier stages to reach the correct frequencies for the transmitting and receiving antennas. The receiver used was a sub-harmonic Schottky diode mixer. The IF signal was amplified by two LNAs. A reference signal was generated by mixing the fundamental signals
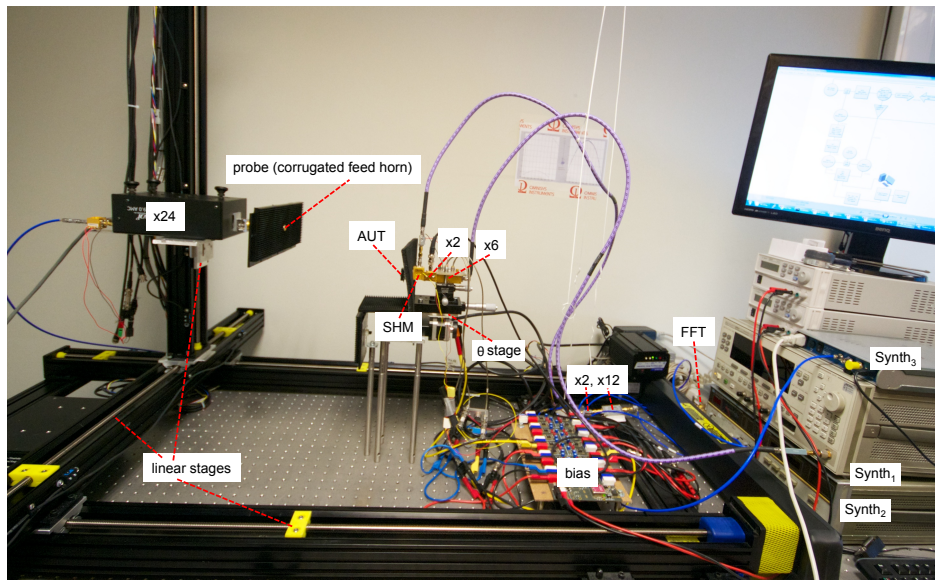
Figure 3.6: Setup for antenna measurements. The configuration being displayed is adjusted for far field measurements (θ cuts) of the smooth walled spline horn at 340 GHz.

from the synthesizers and up-converting the first tone using the same multiplication factor as for the transmitter. By using the same multiplication factor for the up-conversion, a large part of the relative phase drifts were the same for the IF and reference signal. Both signals were finally down-converted using a common source to match the bandwidth of an FFT spectrometer (0-2.5 GHz). A desktop computer was used to control the motion of the linear stages and collecting data from the FFT spectrometer. Radio absorbing material (RAM) with a return loss of < -40 dB was used around the probe and the AUT to minimise unwanted effects of multi-path propagation/standing waves. The probe had chamfered aperture edges for the same reason.

Spontaneous phase variations in the electronics were divided into short-term and long-term drifts. Short term drifts were minimised by carefully choosing stable working points (frequency, bias voltages etc.) for all components in the setup. Long term drifts of the phase were seen to correlate well with the ambient temperature changes, cf. Figure 3.8. It could be seen that long-term phase drifts could be significant but linear if the temperature changed at a constant rate. Thus, lengthy measurements (2-3 hours) were performed during the night when the temperature was seen to change slowly and linearly. A phase reference was taken every 15th minute by moving the probe to boresight and recording the phase. By assuming a linear phase variation, a post-measurement compensation was used to even out the phase drifts.

Mechanical measurements using a flat granite stone as a reference showed that the peak-to-peak deviation in the scanning plane was $\lesssim 70$ μm over a 32 cm $\times$ 32 cm area. However, with a scanning plane of approximately 10 cm $\times$ 10 cm, the mechanical deviations were
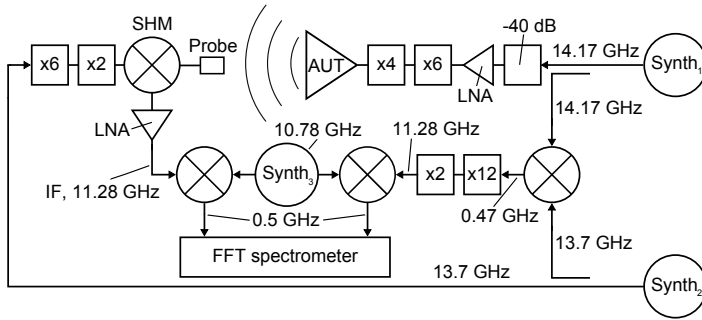
Figure 3.7: Setup used for phase and amplitude measurements of spline horn antennas in the 323-357 GHz range. A sub-harmonic Schottky mixer behind the open-ended waveguide probe was used as a receiver. Schottky multipliers were used for the mixer LO and feeding the AUT. A synthesizer was used for down-conversion to 0.5 GHz to match the bandwidth of the FFT spectrometer.

small enough locally to be neglected at 340 GHz. For the measurements presented below, the measured flatness data was never used to implement a correction matrix for the phase at each grid point.

As shown in Figure 2.20, every horisontal movement is shorter than than the consecutive vertical movements in order to minimise vibrations caused by the larger mass of the vertical linear stage. Since the number of points where the field was typically large ($\sim 10^6$), the movement of the probe had to be done "on-the-fly", i.e. without stops, to make the measurement time reasonably long. In order to avoid any smearing effects when sampling the field, the setup had to be adjusted so that the post- detection integration time was short and the movement of the probe slow.

Bending of the coaxial cables for the mixer LO and IF has been seen to be one of the largest phase error contributors for near field scanners at high frequencies [83]. This problem was handled by choosing phase stable cables with respect to flexure and arranging them for minimum movement/bending.
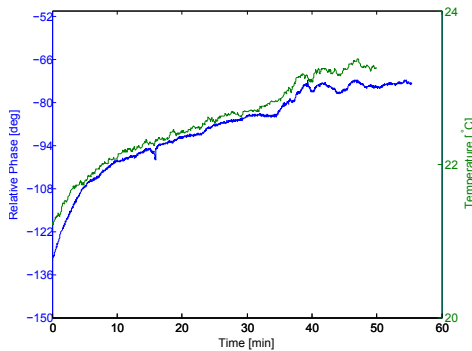

Figure 3.8: Relative phase (left axis) and ambient temperature (right axis) during one hour.

3.3.2 Smooth walled spline feed horns

Measurement results, design and manufacturing procedure for smooth spline feed horn antennas at 340 GHz are presented in paper B. The planar scanner was used for beam measurements to calculate the Gaussicity. However, since a planar scanner has the disadvantage of truncating the field being measured the AUT was mounted on a rotary stage in the far field to enable measurements of side lobes at far out angles.

Figure 3.10 shows results from the planar measurements at 329 GHz. A summary of the calculated table 3.1.

Table 3.1: Gaussian beam parameters for smooth-spline horn calculated from measured data.

Frequency [GHz]	Gaussicity [%]	Waist radius [mm]	Aperture-waist distance [mm]
329	97.7	1.86	12.67
338	97.8	1.94	12.70

Besides having an excellent consistency with simulations (cf. paper B), the results from figure 3.10 also show that the dynamic range of the setup is better than 40 dB and that a highly symmetric phase pattern can be obtained after corrections for linear drifts. Since the signal source used for the transmitting side of the setup had a strong frequency dependence of the output power, it was only possible to perform the beam measurements at 329 and 338 GHz where the signal was strong and stable. At frequencies ≥ 340 GHz, the output power dropped to essentially zero. This signal source was later replaced for the far field θ cuts measurement discussed below.
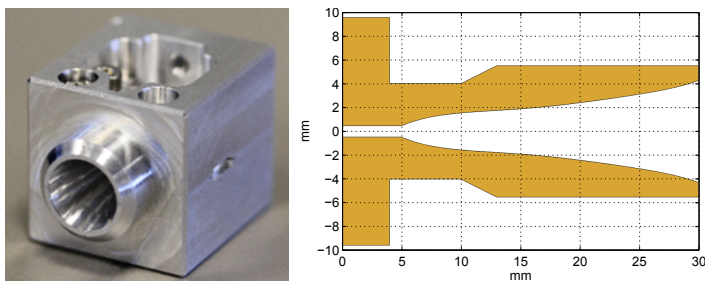

Figure 3.9: Photograph showing a spline horn integrated into a metallic block with WR2.8 input waveguide (left) and figure showing the actual spline profile of the same horn.

The calculation of Gaussicity is sensitive to lateral probe-AUT misalignments. A misalignment in the order of $\lambda/2$ was enough to decrease the calculated Gaussicity of a few percentage points. To counteract this, a post-measurement alignment was made taking the maximum of the power pattern (derived using a polynomial data fit) as the center reference. Having a phase pattern that is simultaneously centered suggests a good rotational alignment of the AUT. This alignment was acheived by first mounting a micrometer gauge on a rod attached to the planar scanner. Using the linear stages, the gauge could be swept along reference surfaces on the horn to measure the pointing error relative to the plane of the scanner. A

large truncation of the measured field tends to lead to an over-estimated Gaussicity calcula-tion as the irregularities seen far away from the main are simply omitted. Hence, a scan area covering a portion of the beam down to below −40 dB was used.

Results from θ scan measurements in the far field at 340 GHz are shown in figure 3.11. Besides having a good agreement between simulations and measurements, it can be seen that side lobes down to -40 dB below the main lobe peak can be resolved. The biggest discrepancy between simulations and measurements can be seen in the H plane, most notably at 340 GHz, where the measured main lobe is wider. Preliminary results from post-measurement analyses suggest that that a mechanical error in the back of the horn (where the transition from straight circular waveguide to spline horn takes place) is the reason for the beam widening. This mechanical error causes a slight difference in the combination of waveguide modes that are launched into the horn structure, which in turn manifests itself as a combination of two different equivalent Gaussian beam modes at different locations inside the horn aperture, and thus a less symmetric beam pattern.
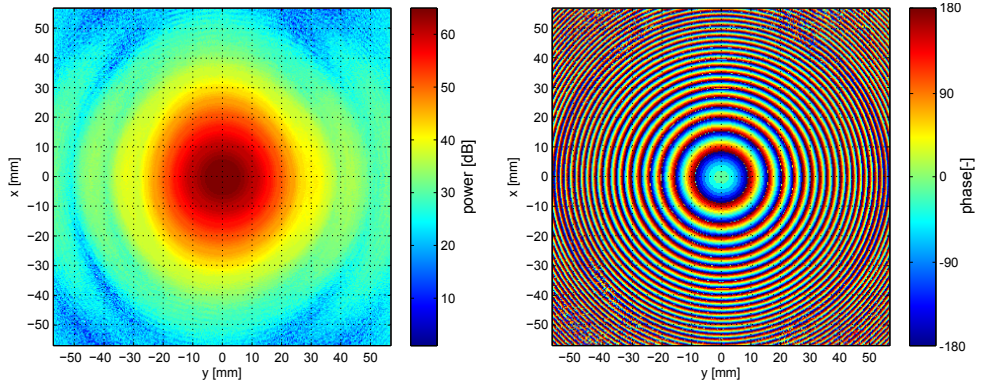

Figure 3.10: Measured power (left) and phase (right) contour plots of smooth walled spline horn at 329 GHz. The H plane is aligned with the vertical x-axis and, consequently, the E plane is aligned with the horisontal y-axis.
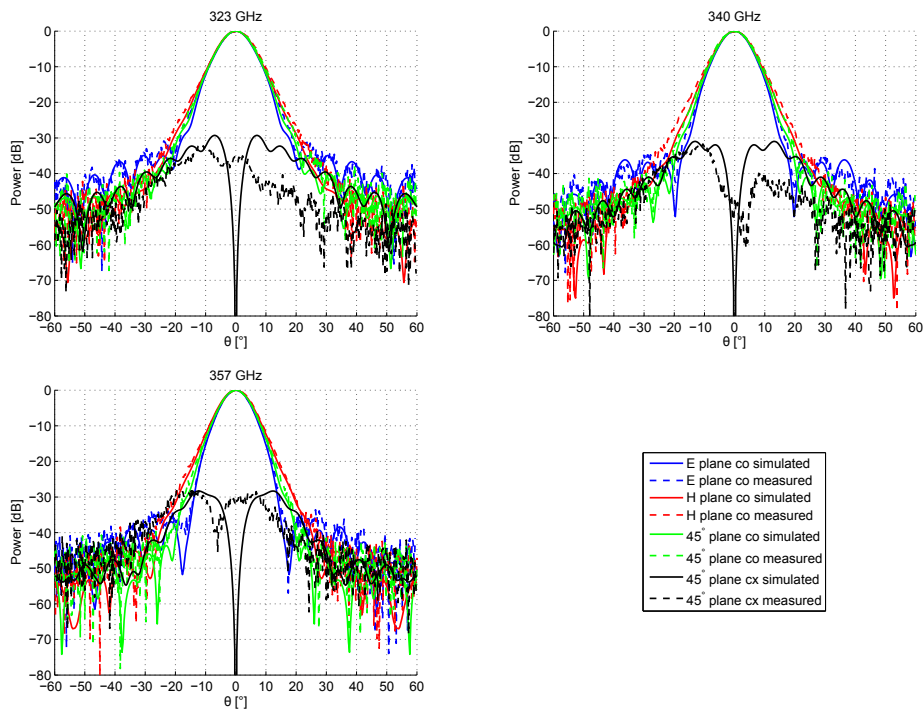
Figure 3.11: θ co-polar power cuts in the E, H and 45° planes and cross-polar cut in the 45° plane of 340 GHz spline horn (far field).

Chapter 4

Conclusion and future outlook

In this thesis, an opto-mechanical tolerance study as well as prototyping and measurements of a smooth-walled spline horn antenna, both for the STEAMR instrument, were presented.

Even though the optical requirements are unique for STEAMR, the methodology used for the tolerance study is general and can be applied for other future multi-beam instruments operating at sub-mm wavelengths. In particular, the separation between pointing and worst-case beam distortion is a practical way of avoiding extremely lengthy simulations for several high-frequency beams using PO/PTD methods. Employing statistical methods for perturbations of all reflectors showed that the performance will be acceptable from manufacturing with overall tolerances of approximately 100 μm. By also studying single-element perturbations, it could be seen that reflectors situated near the focal plane are outstanding in terms of sensitivity to misalignment. Including the manufacturing and mechanical measurements of a demonstrator enabled simplifications in the problem setup for the tolerance analysis as well as confirming that the system can be realised with the tolerances necessary from the analysis.

The experience gained from the mechanical tolerancing study will be used when designing the new STEAMR optics for the ALiSS mission, which includes a new beam layout, calibration optics and an overall more compact design with fewer elements. Using the outlined methodology allows for near field measurements of the demonstrator, which should be used to confirm the accuracy of the manufacturing methods as well as the impact from a deliberatly introduced misalingment.

The smooth-walled spline horn was concluded to be a promising candidate as feed horn for STEAMR. Measurements of the manufactured horns showed a Gaussicity of 97.7% at 329 GHz, which is in excellent agreement with simulations. Albeit some widening of the radiated beam could be seen from the measurements, the influence of system performance was minor and the optical requirements for the retreival functions could be met. Furthermore, the manufacturing technique where a custom-made broach was used proved to be an efficient way to produce many horns with high repeatability.

This work shows that it is possible to manufacture compact spline horns operating with good performance over a moderate (10%) bandwidth. Previous published work show spline horns having a bandwidth that is larger than that for a standard corrugated feed horn. It is

therefore interesting to make a more detailed investigation of what trade-offs exist for physical dimensions versus performance over larger bandwidths for the smooth-walled spline horn. A mechanical tolerance study is also an important task since it will help clarifying which manufacturing methods are the most appropriate. Prototyping horns for use above 1 THz is also interesting since difficulties in fabrication of corrugated horns at such high frequencies pose a major problem.

To conclude, it has been the aim of the work presented in this thesis to highlight the practical aspects of developing optical systems operating at THz frequencies. An approach where methods of modern simulation software are combined with concurrent engineering between hardware manufacturing/test measurements seems to be an efficient way to increase system reliability and driving down costs. It is the hope of the author that this line of action will be useful in the realisation of future instruments for astronomy/atmospheric research and ease implementation of the technology for new applications.

Chapter 5

Summary of appended papers

Paper A

Optical Tolerance Analysis of the Multi-Beam Limb Viewing Instrument STEAMR

This paper deals with a mechanical tolerance analysis for the STEAMR instrument. Methods of ray-tracing and physcial optics were used to investigate the impact of reflector misalignment, both from a statistical point of view and by means of single element perturbations. Distortions of the 1.6 m × 0.8 m primary reflector surface were also investigated. A demonstrator representing a full-sized sub-system of the optical chain was manufactured and measured mechanically. The results from these measurements were input into the software used for simulation to confirm that the manufacturing methods were accurate enough.

The author's contributions included setting up optical models in two separate software programs, compiling and analysing the simulation data and writing the article.

Paper B

A 340 GHz High Gaussicity Smooth Spline Horn Antenna for the STEAMR Instrument

In this paper, a compact smooth-walled spline horn at 340 GHz is presented as a promising candidate as feed horns for the STEAMR instrument. The optimisation proceses for designing the horn and the manufacturing methods are explained.

The author's foremost contribution was to build the measurement setup for planar and spherical antenna measurements as well as performing the actual measurements. Subsequent analysis, including investigating the performance implications for the STEAMR instrument and writing the article were also done by the author.

References

[1] B. Carnicero Dominguez *et al.*, "ESA's premier mission candidate: System and pay-load overview," in *Geoscience and Remote Sensing Symposium (IGARSS), 2012 IEEE International*, 2012, pp. 5538–5541.

[2] T. Phillips and J. Keene, "Submillimeter astronomy [heterodyne spectroscopy]," *Proceedings of the IEEE*, vol. 80, no. 11, pp. 1662–1678, Nov 1992.

[3] "ESA website." [Online]. Available: http://www.esa.int/Our_Activities/Observing_the_Earth/Earth_Explorers_overview

[4] P. Edwards and D. Pawlak, "Metop: The space segment for Eumetsat's polar system," *ESA Bull.*, no. 102, pp. 6–18, May 2000.

[5] U. Frisk *et al.*, "The Odin satellite. I. Radiometer design and test," *Astronomy and Astrophysics*, vol. 402, pp. L27–L34, May 2003.

[6] P. Goldsmith, "Focal plane arrays for millimeter-wavelength astronomy," in *IEEE MTT-S International Microwave Symposium Digest, 1992.*, June 1992, pp. 1255–1258 vol.3.

[7] J. Waters and G. Peckham, "The microwave limb sounder (MLS) experiments for UARS and EOS," in *Geoscience and Remote Sensing Symposium, 1991. IGARSS '91. Remote Sensing: Global Monitoring for Earth Management., International*, vol. 2, Jun 1991, pp. 543–546.

[8] F. T. Barath *et al.*, "The Upper Atmosphere Research Satellite microwave limb sounder instrument," *J. Geophys. Res.*, vol. 98, no. 6, pp. 10 751–10 762, 1993.

[9] C. Croskey *et al.*, "The Millimeter Wave Atmospheric Sounder (MAS): a shuttle-based remote sensing experiment," *IEEE Transactions on Microwave Theory and Techniques*, vol. 40, no. 6, pp. 1090–1100, Jun 1992.

[10] Y. Kasai, J. Urban, C. Takahashi, S. Hoshino, K. Takahashi, J. Inatani, M. Shiotani, and H. Masuko, "Stratospheric ozone isotope enrichment studied by submillimeter wave heterodyne radiometry: the observation capabilities of SMILES," *IEEE Transactions on Geoscience and Remote Sensing*, vol. 44, no. 3, pp. 676–693, March 2006.

[11] J. Urban, P. Baron, N. Lautie, N. Schneider, K. Dassas, P. Ricaud, and J. D. L. Noe, "Moliere (v5): a versatile forward- and inversion model for the millimeter and sub-millimeter wavelength range," *Journal of Quantitative Spectroscopy and Radiative Transfer*, vol. 83, no. 3-4, pp. 529 – 554, 2004.

[12] P. Eriksson, "Microwave radiometric observations of the middle atmosphere: simulations and inversions," PhD thesis, 1999.

[13] P. Goldsmith, *Quasioptical Systems: Gaussian Beam Quasioptical Propogation and Applications*, ser. IEEE Press Series on RF and Microwave Technology.   Wiley, 1998.

[14] ——, "Quasi-optical techniques," *Proceedings of the IEEE*, vol. 80, no. 11, pp. 1729–1747, Nov 1992.

[15] G. L. Stephens *et al.*, "The cloudsat mission and the a-train - a new dimension of space-based observations of clouds and precipitation," *Bulletin of the American Meteorological Society*, vol. 83, pp. 1771–1790, dec 2002.

[16] T. Bryllert, K. Cooper, R. Dengler, N. Llombart, G. Chattopadhyay, E. Schlecht, J. Gill, C. Lee, A. Skalare, I. Mehdi, and P. Siegel, "A 600 GHz imaging radar for concealed objects detection," in *Radar Conference, 2009 IEEE*, May 2009, pp. 1–3.

[17] D. Woolard, E. Brown, M. Pepper, and M. Kemp, "Terahertz frequency sensing and imaging: A time of reckoning future applications?" *Proceedings of the IEEE*, vol. 93, no. 10, pp. 1722–1743, Oct 2005.

[18] P. Siegel, "Terahertz technology in biology and medicine," in *Microwave Symposium Digest, 2004 IEEE MTT-S International*, vol. 3, June 2004, pp. 1575–1578 Vol.3.

[19] S. Kharkovsky, J. Case, R. Zoughi, and F. Hepburn, "Millimeter wave detection of localized anomalies in the space shuttle external fuel tank insulating foam and acreage heat tiles," in *Instrumentation and Measurement Technology Conference, 2005. IMTC 2005. Proceedings of the IEEE*, vol. 2, May 2005, pp. 1527–1530.

[20] R. Piesiewicz, M. N. Islam, M. Koch, and T. Kurner, "Towards short-range terahertz communication systems: Basic considerations," in *18th International Conference on Applied Electromagnetics and Communications, 2005. ICECom 2005.*, Oct 2005, pp. 1–5.

[21] A. Wootten and A. Thompson, "The Atacama Large Millimeter/Submillimeter Array," *Proceedings of the IEEE*, vol. 97, no. 8, pp. 1463–1471, Aug 2009.

[22] M. Griffin, G. Pilbratt, T. de Graauw, and A. Poglitsch, "The Herschel Space Observatory," in *Infrared, Millimeter and Terahertz Waves, 2008. IRMMW-THz 2008. 33rd International Conference on*, Sept 2008, pp. 1–2.

[23] D. Doyle, G. Pilbratt, and J. Tauber, "The herschel and planck space telescopes," *Proceedings of the IEEE*, vol. 97, no. 8, pp. 1403–1411, Aug 2009.

[24] N. W. Boggess *et al.*, "The COBE mission - Its design and performance two years after launch," *Astrophysical Journal*, vol. 397, pp. 420–429, Oct. 1992.

[25] J. Kumagal, "Space mountain [submillimeter radio telescopes]," *Spectrum, IEEE*, vol. 42, no. 12, pp. 12–14, Dec 2005.

[26] P. Siegel, "THz Instruments for Space," *IEEE Transactions on Antennas and Propagation*, vol. 55, no. 11, pp. 2957–2965, Nov 2007.

[27] The Royal Observatory, Edinburgh website. [Online]. Available: http://www.roe.ac.uk/roe/support/pr/picturegallery/herschel.jpg

[28] OHB Sweden website. [Online]. Available: http://www.ohb-sweden.se/sites/default/files/Odin5.jpg

[29] "ESA website." [Online]. Available: http://blogs.esa.int/rocketscience/files/2012/10/InstrumentCloseUp_Alpha.jpg

[30] Wikipedia website. [Online]. Available: http://upload.wikimedia.org/wikipedia/commons/b/b4/ALMA_and_a_Starry_Night.jpg

[31] R. M. Goody and Y. L. Yung, *Atmospheric radiation: theoretical basis*. New York: Oxford University Press New York, 1989.

[32] C. A. Balanis, *Antenna theory: analysis and design*. Wiley, 2005.

[33] D. B. Rutledge, *The electronics of radio*. Cambridge: Cambridge University Press, 1999.

[34] N. Skou and D. M. Le Vine, *Microwave radiometer systems: design and analysis*. Boston: Artech House, 2006.

[35] D. Allan, "Statistics of atomic frequency standards," *Proceedings of the IEEE*, vol. 54, no. 2, pp. 221–230, Feb 1966.

[36] P. Ade *et al.*, "Planck 2013 results. VI. High Frequency Instrument data processing," 2013.

[37] W. Shan, S. Shi, T. Matsunaga, M. Takizawa, A. Endo, T. Noguchi, and Y. Uzawa, "Design and development of sis mixers for alma band 10," *IEEE Transactions on Applied Superconductivity*, vol. 17, no. 2, pp. 363–366, June 2007.

[38] W. Shan, T. Noguchi, S. Shi, and Y. Sekimoto, "Design and development of SIS mixers for ALMA band 8," *IEEE Transactions on Applied Superconductivity*, vol. 15, no. 2, pp. 503–506, June 2005.

[39] S. Cherednichenko, V. Drakinskiy, T. Berg, P. Khosropanah, and E. Kollberg, "Hot-electron bolometer terahertz mixers for the Herschel Space Observatory," *Review of Scientific Instruments*, vol. 79, no. 3, pp. 034 501–034 501–10, Mar 2008.

[40] D. Meledin *et al.*, "A 1.3-THz balanced waveguide HEB mixer for the APEX telescope," *IEEE Transactions on Microwave Theory and Techniques*, vol. 57, no. 1, pp. 89–98, Jan 2009.

[41] H. Zhao, V. Drakinskiy, P. Sobis, J. Hanning, T. Bryllert, A.-Y. Tang, and J. Stake, "Development of a 557 GHz GaAs monolithic membrane-diode mixer," in *2012 International Conference on Indium Phosphide and Related Materials (IPRM)*, Aug 2012, pp. 102–105.

[42] P. Sobis, A. Emrich, and J. Stake, "A low VSWR 2SB schottky receiver," *IEEE Transactions on Terahertz Science and Technology*, vol. 1, no. 2, pp. 403–411, Nov 2011.

[43] P. Siegel, R. Smith, M. Graidis, and S. Martin, "2.5-THz GaAs monolithic membrane-diode mixer," *IEEE Transactions on Microwave Theory and Techniques*, vol. 47, no. 5, pp. 596–604, May 1999.

[44] H. Friis, "A note on a simple transmission formula," *Proceedings of the IRE*, vol. 34, no. 5, pp. 254–256, May 1946.

[45] Y. Rahmat-Samii, R. Hoferer, and H. Mosallaei, "Beam efficiency of reflector antennas: the simple formula," *IEEE Antennas and Propagation Magazine*, vol. 40, no. 5, pp. 82–87, Oct 1998.

[46] R. N. Wilson, *Reflecting telescope optics I: basic design theory and its historical development*.   New York; Berlin: Springer, 2004.

[47] NASA hubble website. [Online]. Available: http://hubblesite.org/

[48] ESO website. [Online]. Available: http://www.eso.org/public/teles-instr/vlt/

[49] M. Lampton and M. Sholl, "Comparison of on-axis three-mirror-anastigmat telescopes," *Proc. SPIE*, vol. 6687, pp. 66 870S–66 870S–8, 2007.

[50] C. Dragone, "Offset multireflector antennas with perfect pattern symmetry and polarization discrimination," *Bell System Technical Journal, The*, vol. 57, no. 7, pp. 2663–2684, Sept 1978.

[51] Y. Mizugutch, M. Akagawa, and H. Yokoi, "Offset dual reflector antenna," in *Antennas and Propagation Society International Symposium, 1976*, vol. 14, Oct 1976, pp. 2–5.

[52] M. Born and E. Wolf, *Principles of Optics*, 7th ed.   Cambridge University Press, 1999.

[53] P. S. Kildal, *Foundations of antennas: a unified approach*.   Lund: Studentlitteratur, 2000.

[54] A. Bondeson, T. Rylander, and P. Ingelstrom, *Computational electromagnetics*.   New York; London: Springer, 2012, vol. 51; 51.

[55] P. D. Potter, "A new horn antenna with suppressed sidelobes and equal beamwidths," *Microwave journal*, vol. VI, pp. 71–78, June 1963.

[56] J. F. Johansson, "A Comparison of Some Feed Types," in *Multi-Feed Systems for Radio Telescopes*, ser. Astronomical Society of the Pacific Conference Series, vol. 75, 1995, p. 82.

[57] J. McKay, D. Robertson, P. Cruickshank, R. Hunter, D. Bolton, R. Wylde, and G. Smith, "Compact wideband corrugated feedhorns with ultra-low sidelobes for very high performance antennas and quasi-optical systems," *IEEE Transactions on Antennas and Propagation*, vol. 61, no. 4, pp. 1714–1721, April 2013.

[58] A. Gonzalez and Y. Uzawa, "Tolerance analysis of alma band 10 corrugated horns and optics," *IEEE Transactions on Antennas and Propagation*, vol. 60, no. 7, pp. 3137–3145, July 2012.

[59] E. De Rijk, A. Macor, J. P. Hogge, S. Alberti, and J.-P. Ansermet, "Note: Stacked rings for terahertz wave-guiding," *Review of Scientific Instruments*, vol. 82, no. 6, pp. 066 102–066 102–3, Jun 2011.

[60] C. Granet, G. L. James, R. Bolton, and G. Moorey, "A smooth-walled spline-profile horn as an alternative to the corrugated horn for wide band millimeter-wave applications," *IEEE Transactions on Antennas and Propagation*, vol. 52, no. 3, pp. 848–854, March 2004.

[61] E. Brundermann, H.-W. Hubers, and M. F. Kimmitt, "Terahertz techniques," vol. 151, 2012.

[62] J. Tuovinen, "Accuracy of a gaussian beam," *IEEE Transactions on Antennas and Propagation*, vol. 40, no. 4, pp. 391–398, Apr 1992.

[63] Radiant zemax website. [Online]. Available: http://www.radiantzemax.com/en

[64] Synopsys optical solutions website. [Online]. Available: http://optics.synopsys.com/codev/

[65] TICRA website. [Online]. Available: http://www.ticra.com/products/software/grasp

[66] K. Pontoppidan. GRASP, technical description. Copenhagen; Denmark. [Online]. Available: http://www.ticra.com/

[67] A. Cerboni, P. Brachat, and R. Behe, "Antenna R&D at France Telecom: the CNET Laboratory in La Turbie," *IEEE Antennas and Propagation Magazine*, vol. 36, no. 1, pp. 7–15, Feb 1994.

[68] S. Gregson and I. D. Library, *Principles of Planar Near-Field Antenna Measurements*. Stevenage: IET, 2007.

[69] Space industry news website. [Online]. Available: http://spaceindnews.wpengine.netdna-cdn.com/wp-content/uploads/2014/03/Compact_Payload_Test_Range.jpg

[70] T. Hirvonen, J. Ala-Laurinaho, J. Tuovinen, and A. Raisanen, "A compact antenna test range based on a hologram," *IEEE Transactions on Antennas and Propagation*, vol. 45, no. 8, pp. 1270–1276, Aug 1997.

[71] J. Ala-Laurinaho, T. Hirvonen, P. Piironen, A. Lehto, J. Tuovinen, A. Raisanen, and U. Frisk, "Measurement of the Odin telescope at 119 GHz with a hologram-type CATR," *IEEE Transactions on Antennas and Propagation*, vol. 49, no. 9, pp. 1264–1270, Sep 2001.

[72] A. Karttunen, J. Ala-Laurinaho, M. Vaaja, T. Koskinen, J. Hakli, A. Lonnqvist, J. Mallat, A. Tamminen, V. Viikari, and A. Raisanen, "Antenna Tests With a Hologram-Based CATR at 650 GHz," *IEEE Transactions on Antennas and Propagation*, vol. 57, no. 3, pp. 711–720, March 2009.

[73] NSI website. [Online]. Available: http://ww2.nearfield.com/sales/datasheets/images/NSI-100V-1x1.jpg

[74] Nearfield Systems Inc. website. [Online]. Available: http://www.nearfield.com/

[75] M. Whale, A. Murphy, A. Murk, M. Renker, U. Frisk, and O. Janson, "A Compensating Anastigmatic Submillimeter Array Imaging System for STEAMR," *IEEE Transactions on Terahertz Science and Technology*, vol. 3, no. 1, pp. 110–119, 2013.

[76] M. Whale, M. Renker, A. Murk, U. Frisk, O. Janson, L. Blecha, G. Paciotti, G. Bell, R. Wylde, and A. Muprhy, "The STEAMR instrument: Optical design, develop-ment and testing," in *Proceedings, 23rd International Symposium on Space Terahertz Technology*, Tokyo, Japan, Apr. 2012, pp. 89–92. [Online]. Available: http://www.nrao.edu/meetings/isstt/papers/2012/2012089092.pdf

[77] M. Renker, M. Whale, and A. Murk, "Antenna simulations and measurements of focal plane array facet reflectors," *IEEE Transactions on Antennas and Propagation*, vol. 61, no. 4, pp. 1722–1732, 2013.

[78] M. Renker, "The Stratosphere-Troposphere Exchange And Climate Monitor Radiometer (STEAMR): Optical Design, Radiometric Tests and First Atmospheric Observations," PhD thesis, 2014.

[79] P. Sobis, N. Wadefalk, A. Emrich, and J. Stake, "A Broadband, Low Noise, Integrated 340 GHz Schottky Diode Receiver," *IEEE Microwave and Wireless Components Letters*, vol. 22, no. 7, pp. 366–368, July 2012.

[80] P. Sobis, "Advanced Schottky Diode Receiver Front-Ends for Terahertz Applications," PhD thesis, 2011.

[81] A. Wagner-Gentner, U. Graf, M. Philipp, and D. Rabanus, "A simple method to design astigmatic off-axis mirrors," *Infrared Physics & Technology*, vol. 50, no. 1, pp. 42–46, 2007.

[82] M. H. Kalos and P. A. Whitlock, *Monte Carlo methods*. Weinheim: Wiley-Blackwell, 2008.

[83] D. Slater *et al.*, "A large aperture 650 GHz near-field measurement system for the earth observing system microwave limb sounder," *Antenna Measurement Techniques Association Conf. 20th ESTEC Antenna Workshop on Millimeter Wave Antenna*, Oct 2001.

THANK YOU MARIO!

BUT OUR PRINCESS IS IN
ANOTHER CASTLE!